A stress-sensing C9ORF72-SMCR8 switch licenses FIP200 condensates for rapid mitophagy

Dan Tang[1,2,9], Hui Bao[1,9], Shijian Feng[1,2,9], Wei Chen[1,9], Hang Ci[1,9], Haiying Zhang[1], Xi Jin[1], Liangting Xu[1], Xinjun Zhao[1], Yu Liu[1,3], Qiuxiao Shi[4], Xiaofang Huang[1], Liping Su[1], Lunzhi Dai[1], Wei Cheng[1,7], Lei Gao[8], Biao Dong[3,8], Xiaohe Tian[1], Jing Chen[5], Haoyang Cai[1]*, Kunjie Wang[1]*, Zhonghan Li[1,2]*, Shiqian Qi[1,2,6]*

[1]Department of Urology, Institute of Urology, State Key Laboratory of Biotherapy, West China Hospital, College of Life Sciences, Sichuan University, and National Collaborative Innovation Center, Chengdu, 610041, China;
[2]Frontiers Medical Center, Tianfu Jincheng Laboratory, Chengdu, 610212, China;
[3]National Clinical Research Center for Geriatrics and State Key Laboratory of Biotherapy, West China Hospital, Sichuan University, Chengdu, 610041, China;
[4]Histology and Imaging Platform, Core Facilities of West China Hospital, Sichuan University, Chengdu, 610041, China;
[5]Department of Pediatric Surgery and Laboratory of Pediatric Surgery, West China Hospital, Sichuan University, Chengdu, 610041, China;
[6]Cardiac Structure and Function Research Key Laboratory of Sichuan Province, West China Hospital, Sichuan University, Chengdu, 610041, China;
[7]Sichuan Industrial Institute of Antibiotics, School of Pharmacy, Chengdu University, 610106, Chengdu China;
[8]Sichuan Real & Best Biotech Co., Ltd, Chengdu, 610219, China;
[9]These authors contributed equally to this work.

*Corresponding authors: qishiqian@scu.edu.cn; Zhonghan.li@outlook.com; wangkj@scu.edu.cn; haoyang.cai@scu.edu.cn.

Abstract: Acute mitochondrial damage demands rapid and spatially restricted quality control, yet how cells convert such stress into immediate mitophagic responses remains elusive. Here, we identify the C9ORF72-SMCR8 complex as a phosphorylation-gated molecular switch that couples mitochondrial damage to rapid mitophagy through regulated protein condensation. Ischemic stress induces transient upregulation of C9ORF72, which stabilizes SMCR8 and licenses its effector function. Upon mitochondrial damage, ULK1 phosphorylates SMCR8 at Ser471, enabling engagement with the FIP200 Claw domain and licensing FIP200 condensation at damaged mitochondria. These condensates nucleate mitophagosome biogenesis, thereby promoting rapid and spatially restricted mitochondrial clearance. Disruption of this switch impairs FIP200 condensation and exacerbates ischemic injury *in vivo*. Conversely, a minimal SMCR8-derived peptide is sufficient to reconstitute FIP200 condensate formation, restore mitophagy, and support tissue protection *in vivo*. Together, these findings define a phosphorylation-controlled condensate mechanism in which an intrinsically disordered region in SMCR8 couples mitochondrial stress to rapid mitophagy.

Introduction

Ischemia-reperfusion injury (IRI) underlies a wide range of pathological conditions, including stroke, myocardial infarction, acute kidney injury (AKI), and organ transplantation, and remains a major cause of morbidity and mortality worldwide[1-6]. A unifying lethal event across these conditions is the explosive mitochondrial damage triggered by ischemia and amplified upon reperfusion, including calcium overload, opening of the mitochondrial permeability transition pore, and massive reactive oxygen species generation, which together initiate cascades of necroptosis, apoptosis, and inflammation[7-10]. Although mitochondrial damage occurs within minutes of ischemia and reperfusion, how cells sense this acute stress and activate protective quality-control mechanisms *in vivo* remains incompletely understood[7, 11].

Mitophagy, the selective removal of damaged mitochondria, is a central mechanism for maintaining mitochondrial homeostasis and limiting tissue injury[11-13]. Genetic or pharmacological enhancement of mitophagy confers robust protection across multiple preclinical models of IRI[14-16]. However, mitophagy must be precisely timed: delayed or insufficient activation fails to prevent irreversible damage, whereas excessive activation can be detrimental[17]. Notably, most known mitophagy-enhancing strategies act indirectly through transcriptional or metabolic remodeling and require hours to days to reach efficacy[18, 19]. Thus, a fundamental unresolved question is how cells achieve rapid and spatially confined mitophagy in response to acute mitochondrial damage.

The C9ORF72-SMCR8 complex is best known for its involvement in amyotrophic lateral sclerosis (ALS) and frontotemporal dementia (FTD), where massive G_4C_2 hexanucleotide repeat expansions in *C9ORF72* drive neurodegeneration[20, 21]. However, the physiological functions of the wild-type complex remain poorly understood, particularly outside chronic neurodegenerative contexts[22-24]. While the complex has been implicated in autophagy regulation[25-29], whether it participates in acute stress responses and contributes to mitochondrial quality control has not been examined.

To explore this possibility, we systematically re-analyzed public single-cell and bulk RNA-sequencing datasets from models of ischemic stroke (mouse and rat)[30, 31], myocardial infarction (mouse)[32], and acute kidney injury (mouse, human)[33, 34]. Across species and organs, *C9ORF72* exhibited a conserved, transient induction during the acute phase of injury. This tightly regulated expression pattern suggested that the C9ORF72-SMCR8 (CS) complex may function as a stress-responsive module during acute mitochondrial damage.

Here, we identify the CS complex as a phosphorylation-gated molecular switch that couples mitochondrial damage to rapid mitophagy through regulated protein condensation. Mechanistically, ULK1-dependent phosphorylation of SMCR8 licenses its interaction with the FIP200 Claw domain, triggering stress-induced condensation of FIP200 at damaged mitochondria. This process spatially restricts autophagosome initiation and enables rapid mitochondrial clearance. A minimal 91-residue SMCR8-derived peptide is sufficient to reconstitute this condensate-coupled mitophagy pathway *in vivo*. More broadly, our findings define a phosphorylation-controlled condensate mechanism through which an intrinsically disordered region in SMCR8 couples mitochondrial stress to selective autophagy.

Results

C9ORF72 induction defines a stress-responsive module in ischemic injury

To identify conserved regulators of acute IRI, we re-analyzed publicly available single-cell and single-nucleus RNA-sequencing datasets from mouse[30] and rat brain (snRNA-seq) [31], mouse heart[32], mouse kidney[33], and human kidney (scRNA-seq)[34]. Cross-species, cross-organ integration revealed a small set of genes consistently induced by ischemic stress (Fig. 1a). Among these, *C9ORF72* emerged as one of the most reproducibly induced genes, prompting further investigation.

Spatial transcriptomics of ischemic mouse brain confirmed localized upregulation of *C9orf72* within injured regions, together with other conserved IRI-responsive genes (Fig. 1b). Across models, *C9ORF72* expression displayed a transient, stress-associated induction, peaking early after reperfusion in mouse cerebral IRI, rat cerebral IRI, mouse cardiac and renal IRI, and human kidney transplantation-associated IRI (Fig. 1c,d; Fig. S1a-c). This conserved temporal pattern suggested that *C9ORF72* functions as an early stress-responsive factor during acute ischemic injury.

To determine whether *C9ORF72* induction is protective or detrimental, we generated tissue-specific *C9orf72* conditional knockout (C9 cKO) mice, targeting neural stem cells[35] for cerebral IRI and renal tubular epithelial cells[36] for renal IRI (r-IRI) (Fig. 1e, S1d). In r-IRI (Fig. 1e, S1d), C9 cKO mice significantly worsened renal function, with elevated serum creatinine (CREA) and blood urea nitrogen (BUN), accompanied by aggravated tubular injury and higher histopathological scores compared with WT controls (Fig. 1f-i). Similarly, in the middle cerebral artery occlusion (MCAO) model (Fig. 1e, S1d), laser speckle imaging confirmed occlusion (Fig. S1e-g). C9 cKO mice showed increased infarct volume and severe neurological deficits, including impaired motor coordination and strength (Fig. 1j-n). Histological analyses revealed extensive neuronal loss in ischemic brain regions (Fig. 1o). Thus, loss of *C9orf72* exacerbates ischemic injury in both brain and kidney, establishing *C9ORF72* as a protective factor during acute IRI.

Notably, transmission electron microscopy (TEM) revealed markedly increased mitochondrial damage in ischemic brains of C9 cKO mice (Fig. 1p). Consistently, pathway enrichment analysis of ischemia-induced genes highlighted mitochondrial and lipid metabolic pathways, including autophagy and mitophagy (Fig. 1q, S1h). Together, these results identify *C9ORF72* as a conserved stress-responsive factor whose induction correlates with mitochondrial damage and tissue injury across organs.

SMCR8 functions as the effector module linking stress sensing to mitophagy

To determine whether the protective effect of *C9ORF72* is mediated through mitochondrial clearance, we directly assessed stress-induced mitophagy. Because C9ORF72 and SMCR8 mutually stabilize each other, such that loss of C9ORF72 secondarily reduces SMCR8 protein levels (Fig. 2a)[25, 37, 38], single-gene knockouts cannot distinguish direct effector functions from

indirect destabilization effects. We therefore generated *C9ORF72-SMCR8* double knockout (DKO) cells to isolate the intrinsic contribution of each component (Fig. 2b).

To quantify mitophagy, we focused on the Parkin-dependent pathway and established HeLa cell lines stably expressing Flag-Parkin together with the mitochondrial reporter mt-mKeima, a pH-sensitive fluorophore that shifts excitation from 488 nm in neutral mitochondria to 561 nm upon lysosomal delivery, enabling fluorescence-activated cell sorting (FACS)-based measurement of mitophagic flux (Fig. 2b, S2a,b)[39]. Using this system, we tested whether re-expression of individual CS complex components could restore mitophagy in DKO cells. Upon oligomycin A/antimycin A (O/A) treatment, re-expression of SMCR8, but not C9ORF72, robustly increased mitophagic flux (Fig. 2c,d), indicating that SMCR8 is both required and sufficient for efficient Parkin-dependent mitophagy.

Consistent with this conclusion, RNAi-mediated depletion of *SMCR8* in Flag-Parkin/mKeima-expressing HeLa cells markedly suppressed O/A-induced mitophagy (Fig. S2c-e) and impaired the turnover of mitochondrial outer- and inner-membrane proteins, including MFN2, TOM20, and TIM23 (Fig. S2f,g). TEM further revealed a pronounced reduction in mitochondria-engulfing vesicles in *SMCR8*-depleted cells after O/A stimulation under lysosomal inhibition by bafilomycin A1 (Fig. 2e,f).

To determine the physiological relevance of *Smcr8*-mediated mitophagy in tissue protection, we subjected *Smcr8* cKO mice to IRI models (Fig. S2h,i). In r-IRI, *Smcr8* cKO mice exhibited markedly elevated serum CREA and BUN, accompanied by exacerbated tubular damage and higher injury scores compared with WT controls (Fig. 2g-j). Similarly, in MCAO, *Smcr8* cKO mice displayed worsened neurological deficits, increased infarct volumes, and extensive neuronal loss in ischemic brain regions (Fig. 2k-p). Notably, TEM revealed severe mitochondrial fragmentation in *Smcr8* cKO brains following ischemic injury (Fig. 2q).

These results establish SMCR8 as the effector component of the CS complex that is required and sufficient for efficient mitophagy.

SMCR8 engages FIP200 to license condensate formation during mitophagy

To determine how SMCR8 mechanistically enables stress-induced mitophagy, we asked whether SMCR8 directly engages the autophagy scaffold FIP200, a core component of the ULK1 complex that undergoes phase separation during autophagosome initiation. Although the CS complex has been implicated in bulk autophagy[27, 40], its contribution to selective mitophagy has remained unclear. Given the essential role of FIP200 in mitophagy and the destabilization of SMCR8 upon C9ORF72 loss[26, 37, 38], we hypothesized that SMCR8 serves as the primary interface coupling the C9ORF72-SMCR8 sensor to FIP200-dependent condensate formation (Fig. 3a).

To dissect their individual contributions of CS complex subunits, we overexpressed GFP-C9ORF72 or GFP-SMCR8 in WT, C9KO, and S8KO HEK293T cells. Co-IP analyses revealed that SMCR8, but not C9ORF72, robustly associated with endogenous FIP200 across all genetic

backgrounds (Fig. 3b). Thus, while C9ORF72 is required to maintain SMCR8 homeostasis, the physical engagement with the ULK1 complex is mediated directly by SMCR8.

Consistent with this conclusion, GFP-SMCR8 associated with the ULK1 complex in WT cells but failed to do so in *FIP200*-deficient cells, and this interaction was fully restored upon FIP200 re-expression (Fig. S3a). Moreover, FIP200, but not ULK1 or the ATG13-ATG101 subcomplex, pulled down the endogenous CS complex (Fig. S3b), establishing FIP200 as the principal docking site through which SMCR8 engages the ULK1 complex.

FIP200 is essential for mitophagy and undergoes phase separation during autophagosome initiation[41-45]. Upon O/A-induced mitophagy, FIP200 formed dynamic puncta exhibiting rapid fluorescence recovery after photobleaching (FRAP) in WT cells, consistent with liquid-like condensate behavior (Fig. S3c,d). In contrast, FIP200 FRAP were abolished in DKO cells (Fig. S3c,d). Notably, re-expression of SMCR8 alone fully restored both puncta formation and liquid-like dynamics, suggesting that SMCR8 is necessary and sufficient for FIP200 phase separation during mitophagy (Fig. 3c,d; S3c,d).

To further elucidate how SMCR8 promotes FIP200 condensation, we examined the partitioning behavior of reconstituted CS complex components in DKO cells expressing GFP-FIP200. Both the full CS complex and SMCR8 alone strongly enriched within FIP200 condensates, whereas C9ORF72 alone was excluded (Fig. 3e). Consistently, upon O/A treatment, DKO cells exhibited marked reduction in both the number and mean area of FIP200 puncta, whereas SMCR8 re-expression restored condensate formation by significantly increasing both parameters (Fig. 3f,g; S3e-g).

Together, these data define SMCR8 as the molecular link that engages FIP200 and licenses its condensation to initiate mitophagy.

ULK1 phosphorylation of SMCR8 licenses FIP200 condensate formation

To define the molecular basis of SMCR8 engagement with FIP200, we mapped the interaction interface. Truncation analysis in *FIP200* KO HEK293T cells revealed that SMCR8 binds exclusive with the C-terminal Claw domain of FIP200 (Fig. S4a), a module known to recruit autophagy receptors through phosphorylation-regulated FIR motifs[43, 45, 46]. Bioinformatic analysis of SMCR8 identified two candidate FIR-like motifs containing Ser471 and Ser516 as potential phosphorylation sites (Fig. 4a)[46].

Mutational analysis revealed that substitution of Ser471, but not Ser516, markedly impaired SMCR8-FIP200 interaction (Fig. 4b,c). Consistently, LC-MS/MS analysis of SMCR8 purified from O/A-treated HEK293T cells showed robust induction of Ser471 phosphorylation under mitochondrial stress, whereas Ser516 remained unmodified (Fig. 4d,e; Table S1,S2). Deletion of the Ser471-containing FIR region ($SMCR8^{\Delta 467\text{-}479}$) or a broader intrinsically disordered segment ($SMCR8^{\Delta 395\text{-}500}$) abolished FIP200 binding, while a phospho-deficient mutant ($SMCR8^{S471A}$) reduced binding and a phospho-mimetic mutant ($SMCR8^{S471E}$) enhanced it (Fig. S4b,c), establishing Ser471 phosphorylation as a key determinant of FIP200 engagement.

To define the structural basis of this interaction, we solved the crystal structure of the FIP200 Claw domain in complex with a phosphorylated SMCR8 FIR peptide. The structure revealed that SMCR8 pSer471 forms a hydrogen-bonding network with FIP200 residues Arg1573 and Gln1572 (Fig. 4f, S5a-d; Table S3). Consistently, mutation of either Arg1573 and Gln1572 of FIP200 abolished SMCR8 binding, whereas control mutation had no effect (Fig. 4f-h), suggesting a direct, phosphorylation-dependent interaction.

We next sought to identify the kinase responsible for Ser471 phosphorylation. IP-MS followed by targeted validation identified ULK1 as the upstream kinase (Fig. S6a,b; Table S4). Genetic deletion or pharmacological inhibition of ULK1 abolished Ser471 phosphorylation in cells (Fig. 4i,j). Recombinant ULK1 kinase domain phosphorylated WT SMCR8 FIR but not S471A mutant *in vitro*, enabling Claw binding (Fig. S6c). By contrast, TBK1, previously reported to phosphorylate SMCR8 at other sites[47], did not affect Ser471 phosphorylation (Fig. 4i,j).

Ser471 phosphorylation proved necessary for FIP200 phase separation during mitophagy. In S8KO or DKO cells, re-expression of $SMCR8^{WT}$ rescued O/A-induced FIP200 puncta formation, whereas $SMCR8^{S471A}$ failed (Fig. 4k, S7a-e). Quantitative intensity profiling revealed robust enrichment of SMCR8 within FIP200 condensates under stress, while $SMCR8^{S471A}$ remained diffuse (Fig. 4k, S7c). FRAP confirmed $SMCR8^{S471A}$ failed to restore FIP200 puncta fluidity (Fig. 4l,m, S7f,g).

Importantly, Ser471 phosphorylation was also required for mitophagy. In S8KO or DKO cells, re-expression of $SMCR8^{WT}$ or the phospho-mimetic mutant $SMCR8^{S471E}$ fully rescued O/A-induced mitophagy, whereas $SMCR8^{\Delta 467-479}$ or $SMCR8^{S471A}$ failed to do so (Fig. S8a-d). These results indicate that Ser471 phosphorylation is required not only for FIP200 condensation but also for execution of mitophagy.

Functionally, Ser471 phosphorylation spatially coupled autophagosome biogenesis to damaged mitochondria. O/A treatment increased FIP200-mitochondria colocalization in WT COS7 cells but not in DKO or S8KO cells, a defect rescued by SMCR8 but not $SMCR8^{S471A}$ (Fig. S9a-f). LC3-mitochondria association showed a similar pattern (Fig. S9g-l). 3D reconstruction analysis revealed reduced overlap volume between FIP200 puncta and mitochondria in DKO or S8KO cells, restored by SMCR8 but not $SMCR8^{S471A}$ (Fig. 4n,o, S9m-p). Consistently, TEM confirmed that mitochondria-containing vesicles were rescued by SMCR8 but not $SMCR8^{S471A}$ in *SMCR8* KD cells (Fig. 4p,q).

To determine whether the ULK1-SMCR8 phosphorylation switch that gates FIP200 phase separation is required for tissue protection *in vivo*, we next assessed the physiological consequences of selectively disrupting this interaction. Because mutation of SMCR8 at Ser471 abolishes FIP200 engagement and mitophagy in cells, we leveraged this phosphorylation-deficient mutant to directly test whether the same molecular switch underlies protection against IRI at the organismal level.

We therefore performed AAV-mediated rescue experiments in *Smcr8* cKO mice subjected to r-IRI and MCAO. Expression of $SMCR8^{WT}$, but not $SMCR8^{S471A}$, dramatically reduced serum CREA and BUN level and preserved tubular architecture following r-IRI (Fig. 5a-e). Similarly,

in MCAO, SMCR8^{WT}, but not SMCR8^{S471A} significantly improved neurological outcome, reduced infarct volume, and rescued mitochondrial ultrastructure in ischemic brain tissue (Fig. 5f-k).

These findings establish Ser471 phosphorylation as a licensing step that enables SMCR8 to engage FIP200 and drive condensate formation.

A minimal SMCR8 module reconstitutes condensate-driven mitophagy

Having established that Ser471 phosphorylation within an intrinsically disordered region (IDR) of SMCR8 licenses FIP200 recruitment, we next sought to define the minimal SMCR8 fragment. Systematic truncation analysis in S8KO cells, assessed by mKeima-based mitophagic flux, revealed that residues 410-500 (SMCR8$^{410\text{-}500}$) represent the shortest segment that fully rescued O/A-induced mitophagy to wild-type levels, whereas shorter constructs or SMCR8$^{410\text{–}500\ S471A}$ mutant were ineffective (Fig. 6a, S10a).

Consistent with its mitophagy activity, SMCR8$^{410\text{-}500}$ also recapitulated stress-induced FIP200 condensation and condensate fluidity in S8KO cells. FRAP revealed kinetics indistinguishable from those observed with full-length SMCR8, whereas SMCR8$^{410\text{-}500\ S471A}$ failed to restore either condensate formation or fluidity (Fig. 6b,c).

We next evaluated the therapeutic potential of this minimal SMCR8 fragment *in vivo*. AAV encoding SMCR8$^{410\text{-}500}$ or SMCR8^{WT} was delivered to kidney or brain of WT mice prior to ischemic injury (Fig. S10b). In r-IRI, expression of either SMCR8^{WT} or SMCR8$^{410\text{-}500}$, markedly reduced serum CREA and BUN levels, attenuated tubular necrosis, and preserved brush-border integrity, whereas the S471A mutant was ineffective (Fig. 6d,e; Fig. S10c,d). Similarly, in MCAO, SMCR8$^{410\text{-}500}$, but not SMCR8$^{410\text{-}500\ S471A}$, recapitulated the neuroprotective effects of SMCR8^{WT}, improving neurological scores, grip strength, and rotarod performance, and decreasing infarct volume (Fig. 6f-h, S10e-g).

Thus, a single phosphorylatable 91-residue SMCR8 peptide is sufficient to drive FIP200 phase separation, mitophagosome biogenesis, and ischemic organ protection (Fig. 6i). These findings establish SMCR8 Ser471 phosphorylation as a modular control point for condensate-coupled mitophagy *in vivo*.

Discussion

The CS complex has long been studied primarily in the context of ALS and FTD, where pathogenic repeat expansions in *C9ORF72* drive chronic neurodegeneration[20, 21, 28, 48, 49]. Here, we identify an unexpected role for the wild-type CS complex in acute stress adaptation. Across organs and species, ischemic stress induces a rapid and transient increase in *C9ORF72* expression, and genetic ablation reveals that this response is protective *in vivo*. Mechanistically, this protection is executed by SMCR8 through mitophagy, rather than through the canonical GEF/GAP-associated functions previously ascribed to the CS complex [37, 50-53].

Our findings define a phosphorylation-gated mitophagy switch in which ULK1-dependent phosphorylation of SMCR8 at Ser471 licenses its interaction with the FIP200 Claw domain and promotes FIP200 condensation at damaged mitochondria. This condensate assembly spatially restricts autophagosome initiation and enables rapid mitophagosome biogenesis in response to mitochondrial damage. In this framework, SMCR8 functions as the effector module linking stress signaling to the core autophagy scaffold, whereas the FIP200 Claw domain acts as a regulatory hub for signal-dependent recruitment[13, 54]. The observation that ULK1 phosphorylates both SMCR8 and FIP200 further supports a model in which kinase signaling coordinates multiple layers of scaffold activation during mitophagy initiation[55-57].

A central mechanistic insight from this study is that the middle intrinsically disordered region (IDR) of SMCR8 as a previously unrecognized regulatory module, distinct from the N-terminal Longin[37, 56, 58, 59] and C-terminal DENN domains[25, 26, 51, 60, 61]. This IDR integrates phosphorylation-dependent signaling with scaffold engagement and condensate formation, thereby providing temporal control and organelle selectivity during acute stress. By contrast, a second FIR-like sequence within SMCR8 is functionally inactive in our assays, indicating that the productive FIP200 engagement and condensate formation requires more than motif resemblance and is constrained by local structural and sequence context.

These findings also provide a mechanistic framework for reconciling acute and chronic phenotypes linked to CS complex dysfunction. In both settings, C9ORF72 loss reduces SMCR8 abundance, however, the consequences differ in timescale and manifestation. In acute IRI, transient stress-induced *C9ORF72* upregulation appears insufficient to sustain SMCR8 availability, rendering SMCR8 function rate-limiting for mitochondrial quality control. In chronic neurodegenerative contexts, persistent *C9ORF72* insufficiency may similarly compromise SMCR8-dependent scaffold engagement and mitophagy over time, thereby contributing to progressive organelle dysfunction[23, 54, 62, 63]. Although these disease settings differ substantially, our data suggest that impaired SMCR8-dependent condensate regulation may represent a shared mechanistic vulnerability.

More broadly, this study identifies a mechanism by which cells translate mitochondrial damage into rapid and spatially restricted organelle quality control. Specifically, phosphorylation of an intrinsically disordered region in SMCR8 directly controls engagement of an autophagy scaffold and thereby regulates local condensate assembly at damaged mitochondria. This mechanism offers a conceptual framework for how cells achieve speed, selectivity, and reversibility in stress responses without requiring global activation of autophagy or slower transcriptional remodeling.

Our findings further indicate that this switch is modular: a minimal phosphorylatable SMCR8-derived peptide is sufficient to reconstitute condensate-coupled mitophagy *in vivo*. This result highlights the tractability of phosphorylation-controlled condensate switches and supports the idea that IDR-based signal integration can be functionally encoded within compact modules. More generally, kinase-regulated scaffold engagement through intrinsically disordered regions may represent a broader strategy for organizing selective quality-control pathways under acute stress.

Methods

Data acquisition and processing

Publicly available single-cell RNA sequencing (scRNA-seq), single-nucleus RNA sequencing (snRNA-seq), and spatial transcriptomics datasets were retrieved from the NCBI Gene Expression Omnibus (GEO). Datasets analyzed in this study included mouse brain spatial transcriptomics (GSE233815), mouse kidney scRNA-seq (GSE180420), mouse heart snRNA-seq (GSE130699), rat brain snRNA-seq (GSE250245), and human kidney scRNA-seq (GSE145927). Raw gene expression matrices were processed using the Seurat R package (v.4.1.0)[64] for quality control and downstream analysis. Low-quality cells/nuclei with high mitochondrial gene content or low feature counts were filtered out based on dataset-specific thresholds. Data were normalized using the NormalizeData function, followed by identification of highly variable features (FindVariableFeatures). Dimensionality reduction was performed using Principal Component Analysis (PCA), and Uniform Manifold Approximation and Projection (UMAP) was used for visualization.

Differential expression and intersection analysis

To identify transcriptomic changes induced by ischemia, differential expression analysis was performed between ischemic and control groups using the FindMarkers function in Seurat. Statistical significance for high-throughput screening was determined using the two-sided Wilcoxon rank-sum test. Upregulated differentially expressed genes (DEGs) were defined based on a Bonferroni-adjusted $P < 0.0001$ and $\log_2 FC > 0.2$.

To identify a conserved ischemic signature, the intersection of upregulated DEGs across the five independent datasets was analyzed. A Venn diagram was generated using the ggvenn R package (v.0.1.19)[65] to visualize the overlap, identifying a core set of 16 consensus genes, notably including *C9ORF72* (*C9orf72* in mouse).

Spatial transcriptomics analysis

Following the identification of C9ORF72 as a conserved core gene in the cross-dataset intersection analysis, a targeted spatial investigation was performed to characterize its local transcriptomic microenvironment. Using the mouse brain spatial transcriptomics dataset (GSE233815), data were first subset to retain only spots exhibiting detectable *C9orf72* expression (defined as normalized counts > 0). These *C9orf72*-positive spots were subsequently stratified based on their spatial coordinates and histological annotations: spots located within the ischemic injury zone were assigned to the ischemic group, while those from sham-operated tissues served as the control group. Targeted differential expression analysis was then conducted specifically between these two spatially defined groups of *C9orf72*-expressing spots to reveal ischemia-induced transcriptional alterations associated with *C9orf72* upregulation.

Functional enrichment analysis

Gene Ontology (GO)[66, 67] biological process and Kyoto Encyclopedia of Genes and Genomes (KEGG)[68, 69] pathway enrichment analyses were performed using the clusterProfiler R package (v.4.12.6)[70]. The input gene lists consisted of significant DEGs identified in the respective datasets. *P*-values were adjusted using the Benjamini–Hochberg (BH) method[71] to control the false discovery rate (FDR). Pathways or terms with an adjusted $P < 0.05$ were considered significantly enriched.

Generation of *C9orf72* or *Smcr8* Conditional Knockout (C9 cKO or *Smcr8* cKO) Mouse Model

Wild-type C57BL6 (B6) mice were purchased from Beijing Vital River Laboratory Animal Technology Co., Ltd. *C9orf72*$^{flox/flox}$ or *Smcr8*$^{flox/flox}$ mice were purchased from Cyagen Biosciences Inc.

Exons 4–5 of *C9orf72* were selected as the conditional knockout region (cKO region). The *C9orf72*$^{flox/flox}$ mice were crossed with mice that express Cre recombinase under the control of the CNS-specific *nestin* promoter and enhancer. *C9orf72*$^{flox/+}$, *Nestin-cre*$^{+}$ mice, which were then mated with *C9orf72*$^{flox/flox}$ mice to generate *C9orf72* $^{flox/flox}$, *Nestin-cre*$^{+}$ mice. Genomic DNA was extracted from tail snips using a PCR sample kit (GDSBio, P9052). Genotyping of the animals was achieved by PCR for the loxP1 sites (5'-*AGCTGAGATTGATAGACACTTGGC*-3' and 5'-*CCTTGAATTTCTATTTCCCGGCAT*-3') and the loxP2 sites (5'-*GTTTGGGTCTGGTTTCTTCTTTCA*-3' and 5'- *TAGCTTCACCAAGTTTTCCCAGTT*-3'), Nestin-Cre recombinase was also verified using primers (5'-*CCTTCCTGAAGCAGTAGAGCA*-3' and 5'-*GCCTTATTGTGGAAGGACTG*-3'). The *C9orf72*$^{flox/flox}$ mice were crossed with *Cdh16-cre* mice to produce *C9orf72* $^{flox/flox}$, *Cdh16-cre*$^{+}$ mice as described above. Genotyping of the animals was achieved by PCR for loxP1 sites, loxP2 sites as well as Cdh16-cre recombinase (5'-*GCAGATCTGGCTCTCCAAAG*-3' and 5'-*AGGCAAATTTTGGTGTACGG*-3').

Exon 1 of *Smcr8* was selected as the conditional knockout region (cKO region). The generation of *Smcr8*$^{flox/flox}$, *Nestin-cre*$^{+}$ and *Smcr8*$^{flox/flox}$, *Cdh16-cre*$^{+}$ mice followed the same strategy as that used for obtaining the *Smcr8* cKO mice described above. Genotyping of the animals was achieved by PCR for the loxP1 sites (5'-*CCTCCGACCAACCCTACATTATTTT*-3' and 5'-*GGGCTCATTGTAAGGTTCTTCCTC*-3') and the loxP2 sites (5'-*AGATACCATGTGAGTATCCTGCTG*-3' and 5'-*ACCTCTGAAGATTTTCACCTCAGT*-3').

All animals were housed in a temperature-controlled facility under pathogen-free conditions and a 12-hour light/dark cycle at 23-25°C with free access to food and water. All animal procedures were performed according to guidelines approved by the ethics committee on animal care at West China Hospital (approved NO.: 20211711A).

Cell Culture

HEK293T, HeLa and COS7 cells were obtained from the National Collection of Authenticated Cell Cultures (Cell Bank of the Chinese Academy of Sciences) and cultured in Dulbecco's modified Eagle's medium (DMEM) containing 2 mM L-glutamine. All the medium was

supplemented with 10% fetal bovine serum (FBS, Gibco) and 100 U/ml penicillin-streptomycin (Gibco). All cells were maintained in a humidified incubator at 37°C with 5% CO_2.

Plasmids and Transfection

DNA templates of *SMCR8* were purchased from Shandong WZ Biosciences Inc., while templates of *C9ORF72*, *FIP200*, *ULK1, ATG13*, *ATG101*, and *Parkin* were synthesized from Wuxi Qinglan Biotech Co. Ltd. Genes were cloned into pEGFP-C1 and/or pFlag-CMV2 vectors. All point mutations were generated using the MUT Express MultiS Fast Mutagenesis Kit V2 (Vazyme). Primers for sub-cloning were designed using sdm-primer-v1.1 python program[72]. All plasmids were constructed by standard cloning methods and confirmed by DNA sequencing. Transient transfection of plasmids was performed using jetPRIME® (polyplus, 101000046) following the manufacturer's instructions.

CRISPR/Cas9 Knockout Cell Lines

Gene knockout cell lines were constructed using the CRISPR/Cas9 method as previously described[73]. The single guide RNA (sgRNA) target sequences used in this study are listed as follows: human and green monkey *C9ORF72* sgRNA: 5'-*AATGGGGATCGCAGCACATA*-3', human and green monkey *SMCR8* sgRNA: 5'-*GATCAGCGCCCCTGACGTAG*-3', human *FIP200* sgRNA: 5'-*CTATGTAAAAACACCTTAGAGG*-3', human *ULK1* sgRNA: 5'-*CAAGTTCGAGTTCTCCCGCAAGG*-3', human *TBK1* sgRNA: 5'-*GCTACTGCAAATGTCTTTCGTGG*-3'. The sgRNA/Cas9 plasmid and homologous recombination template plasmid were co-transfected into cells. After 48 hours post-transfection, cells were selected with 2 μg/ml puromycin or 5 μg/ml Blasticidin for two weeks. Single-cell clones were expanded and knockout confirmation was performed by Western blot (WB).

Lentiviral Production and Transduction

HEK293T cells were seeded on 12-well plates at a density of $2x10^5$ cells per well and cultured overnight. For RNA interference, sense and anti-sense DNA oligonucleotides (Sangon Biotech) were annealed and ligated into transfer plasmid pLKO.1-TRC (Target seq *SMCR8*-shRNA1: 5'-*GCTCTGTGACACTGAATATTT*-3', *SMCR8*-shRNA2: 5'-*GTGACTGCACTGGCTATCTTT*-3'). A mixture of four plasmids, pVSV-G, pGAG and pREV (a gift from Zhonghan Li), along with the transfer plasmids, was transfected into the cells in a 1:2:3:2 ratio using PEI reagent (total 960 ng). Supernatant containing the virus was harvested 48 hours post-transfection, clarified by centrifugation at 4000 rpm for 10 minutes, and either used immediately or stored at -80°C. Lentiviral vectors containing shRNAs were packaged and transduced into HeLa cells with 4 μg/mL polybrene. After a two-week selection period with 5 μg/mL blasticidin, cells were collected for subsequent experiments.

PB (piggyBac transposon) Transfection

Stable cell lines expressing mitochondrial-targeted Keima (by COX8 presequence) and Flag-Parkin were generated using the PiggyBac transposon system. Cells were seeded at a density of 2×10^5 per well in 12-well plates. For each well, 600 ng of the PiggyBac transposon-based

expression vector and 400 ng of pEF1α-PBase were transfected using JetPRIME. One day after transfection, cells were selected with 1 μg/mL puromycin for two weeks. After selection, cells were collected for subsequent experiments.

Protein Expression and Purification

The DNA of human *FIP200* (1404-1594) was subcloned into pHis-parallel2 with an N-terminal His_6-tag followed by a TEV cutting site and a Strep-tag. The DNA of human *FIP200* (1490-1594, N-terminal His_6-MBP-tag), *ULK1* (1-283, N-terminal His_6-tag), *MBP-SMCR8 FIR* variants (461-479, N-terminal His_6-tag) were subcloned into pHis-parallel2 with an N-terminal His_6 or His_6-MBP-tag followed by a TEV cutting site. These proteins were expressed in *E. coli* BL21 (*DE3*) cells induced with 0.2 mM Isopropyl β-d-1-thiogalactopyranoside (IPTG) overnight at 16°C. The supernatants were isolated by centrifuging lysate at 25,000 x g for 30 min at 4°C, then loaded onto Ni-NTA resin (QIAGEN) at 4°C. Target proteins were eluted with buffer containing 25 mM Tris-HCl pH8.0, 150 mM NaCl, 0.5 mM Tris (2-carboxyethyl) phosphine hydrochloride (TCEP-HCl), and 250 mM Imidazole pH8.0 and applied to a Hi-Trap Q HP column. Peak fractions were pooled and digested with TEV protease at 4°C overnight. After removing TEV and His-tag by loading the solution onto Ni-NTA resin, target proteins were further purified using a Superdex 200 10/300 GL column in 25 mM Tris-HCl pH 8.0, 150 mM NaCl and 0.5 mM TCEP-HCl.

Immunoprecipitation and Pulldown Assays

For anti-GFP immunoprecipitation, HEK293T cells (50% confluence) were transfected with the appropriate plasmids with PEI according to the manufacturer's instructions. Cells were collected 24 hours after transfection and lysed in lysis buffer (50 mM Tris pH8.0, 150 mM NaCl, 5% (v/v) glycerol, 0.5% (v/v) TritonX-100) in the presence of protease inhibitors (Selleck) for 30 min on ice. Supernatants were collected by centrifugation at 15000 rpm for 15 min at 4 °C and incubated with GFP-Trap agarose beads (KT health) for 2 hours at 4 °C with rotation. Beads were washed stringently to remove nonspecific binding and denatured using SDS-PAGE sample buffer for WB analysis.

For pulldown assays, amylose beads (NEB) were pre-equilibrated with buffer containing 25 mM Tris pH8.0 and 150 mM NaCl. Purified MBP-SMCR8-FIR variants and strep-$FIP200^{1404-1594}$ were mixed at a molar ratio of 1:2 and incubated with amylose beads at 4 °C for 40 min with rotation. Beads were washed 3 times with buffer containing 25 mM Tris pH8.0, 150 mM NaCl, 0.5% (v/v) NP-40 and eluted with 2×SDS-PAGE sample buffer, followed by SDS–PAGE and WB analysis. *In vitro* phosphorylation of MBP-SMCR8-FIR variants was carried out at 25 °C for 10 min, using ULK1-kinase domain purified from *E. coli* in buffer containing 25 mM Tris 8.0, 150 mM NaCl, 0.5mM TCEP-HCl, 1mM ATP, and 1 mM $MgCl_2$.

Protein Crystallization and Structure Solving

The synthetic peptide SSGEpSIEVLGTEK (p-SMCR8), where pS corresponds to the phosphorylated serine residue, was purchased from the Synpeptide company (Nanjing), with purity >98%. Freshly purified FIP200 (1490–1594) protein (20 mg/ml in 25 mM Tris-HCl pH

8.0, 150 mM NaCl and 0.5 mM TCEP-HCl) was saturated with p-SMCR8 peptide with a molar ratio up to 1:2, and then mixed with equal volumes of reservoir solution containing 0.1 M Phosphate-citrate pH 3.75, 42.5% PEG 300 and 0.6% n-Octyl-β-D-glucoside. Crystals of the protein complexes were obtained through hanging-drop vapor diffusion at 18°C and flash-frozen with liquid nitrogen in well buffer supplemented with 20% glycerol. Diffraction data were collected on BL18U and BL19U at the Shanghai Synchrotron Radiation Facility (SSRF)[74] and subsequently processed using HKL2000[75]. Molecular replacement was carried out with the program PHENIX using published structure (PDB: 6DCE). Model building and refinement were carried out with COOT[76] and PHENIX[77]. All structural representations were generated using PyMOL software[78]. The final structure was determined at a resolution of 1.98 Å. Comprehensive statistics for data collection, structure determination, and refinement are provided in Table S3.

Generation of Antibody against phospho-SMCR8^{S471}

S471 phosphorylation peptide and control peptide were conjugated to bovine serum albumin (BSA) and injected into two rabbits for four times immunization (performed by Gene Universal BioLab). Serum was collected and tested for the affinity to S471 phosphorylation peptide and control peptide. The serum specifically recognized S471 phosphorylation peptide but not the control peptide and was subjected to three successive steps of purification: protein-A affinity purification, S471 phosphorylation peptide-BSA affinity purification, and control peptide-BSA reverse purification (collecting the flow-through that could not bind control peptide). The final purified antibody showed high specificity for S471 phosphorylation peptide.

Western Blot and Antibodies

Cell lysates and extracted proteins in the SDS-PAGE loading buffer were denatured at 95°C for 5 min. Proteins were separated by SDS-PAGE and transferred to the PVDF membrane (Bio-Rad). Membranes were blocked in TBST containing 5% milk for 2 hours and incubated with primary antibodies overnight at 4°C. Appropriate HRP-conjugated secondary antibodies were incubated with membranes. Protein bands were detected by ECL reagent (Millipore) using serial time exposure method with signal saturation avoidance (saturated signal will be labeled with red color in ChemiDoc MP Imaging System, Bio-Rad). Antibodies against C9ORF72 (ab221137), SMCR8 (ab202283) were purchased from Abcam. Antibodies against FIP200 (17250-1-AP), ATG13 (18258-1-AP), ATG101 (26562-1-AP) were purchased from Proteintech. Antibodies against ULK1 (sc-390904) were purchased from Santa Cruz Biotechnology. Antibodies against strep (AE066) were purchased from ABclonal. Anti-Flag antibody (F1084) was purchased from Sigma.

LC-MS/MS Analysis

To confirm the phosphorylation of SMCR8, plasmids expressing N-terminal GFP-tagged SMCR8 were transfected into HEK293T WT cells. GFP-SMCR8 was immunoprecipitated with anti-GFP antibody, and enriched proteins were separated by SDS-PAGE. Gel bands corresponding to GFP-SMCR8 were excised, reduced with DTT (10 mM, 55°C, 60 minutes), alkylated with iodoacetamide (55 mM, room temperature, 45 minutes), and digested with trypsin for mass spectrometry analysis.

To identify kinase targeting SMCR8, HEK293T WT cells were transfected with GFP-tagged SMCR8 alone or co-transfected with GFP-tagged SMCR8 and GFP-tagged C9ORF72. GFP-tagged proteins were then immunoprecipitated with anti-GFP antibody. The enriched proteins were separated in SDS-PAGE gels. Entire gel lanes were excised. Proteins were subjected to reduction with DTT (10 mM, 55°C, 60 min), followed by alkylation with iodoacetamide (55 mM, room temperature, dark, 45 min), prior to trypsin digestion for mass spectrometry analysis.

The tryptically digested peptides were desalted using C18 ZipTip (Millipore). The desalted peptides were re-dissolved in buffer A (0.1% formic acid) and analyzed by a 75 mm × 25 cm analytical column (packed with 120 A˚ and 1.9 mm C18 resin, Dr.Maisch).

LC-MS/MS analysis was performed with a Vanquish Neo UHPLC instrument coupled to an Orbitrap Exploris 480 mass spectrometer (Thermo Fisher Scientific). Peptide samples were analyzed with a 65 min gradient from 3 to 95% buffer B (80% acetonitrile with 0.1% formic acid) at a flow rate of 0.3 µl /min. The data-dependent acquisition (DDA) was performed in positive ion mode. Full MS scans were acquired from m/z 350 to m/z 1,800 range at a resolution of 60,000. The automatic gain control (AGC) value setting was set at 3×10^6, with maximum fill times of 25 ms. For MS/MS scans, the Top 20 most intense precursors were selected with a 1.6 m/z isolation window and fragmented with a normalized collision energy of 27%. The AGC value for MS/MS was set to a target value of 1×10^6, with a resolution of 30000 and a maximum fill time of 50 ms. Precursors with charge states of z = 2-6 or with unassigned charge state were excluded. A dynamic exclusion period for the data-dependent scan was 30 s.

The raw MS files were analyzed using MaxQuant (Version 1.6) against human database (updated on 09/2023, 20,586 sequences). The precursor peptide mass tolerance was set to 10 ppm and a fragment ion mass tolerance was set to 0.02 Da. Two missed trypsin cleavages were allowed. Carbamidomethylation of cysteine was set as fixed modification. Oxidation of methionine, acetylation (protein N-terminal) and protein phosphorylation (STY) were specified as variable modifications.

Fluorescence-Activated Cell Sorting (FACS)

HeLa cells stably expressing mitochondrial-targeted Keima (mKeima) and Flag-Parkin were generated with the PiggyBac transposon system and lentivirus system. 2×10^5 cells were then seeded in 12-well plates, and transfected with 0.4 µg of indicated plasmids. Cells were treated with O/A at various time points before FACS analysis. Quantification of mKeima ratio (561/488) was performed as previously described[72]. Briefly, Measurements of lysosomal mKeima were made using dual-excitation ratiometric pH measurements at 488 (pH 7) and 561 (pH 4) nm lasers with 620/30 nm and 614/20 nm emission filters, respectively. For each sample, 10,000 events were collected and subsequently gated for mKeima/GFP positive cells that were DAPI-negative (DAPI, Beyotime Biotechnology). Data were analyzed using FlowJo.

Fluorescence Recovery After Photobleaching (FRAP)

Cells cultured on 35 mm glass-bottom dishes were transfected with the indicated plasmids for 24 h. FRAP experiments were performed on a Zeiss 900 LSM microscope utilizing a Plan-apochromat 63 x lens with a 1.4 NA and oil immersion. Defined regions were photobleached at 488 nm and the fluorescence intensities in these regions were collected every 2 s and normalized to the initial intensity before bleaching. Image intensity was measured by Mean ROI and further analyzed by GraphPad Prism[79, 80]. Data are shown as the fractional recovery, which refers to the fraction of the difference between the intensity before and immediately after bleaching.

Live Cell Imaging

WT, *SMCR8* KO, or DKO COS7 cells were plated on 35 mm glass-bottom dishes and transfected with mGFP-FIP200 and mCherry-SMCR8 variants. 24 h later, cells were treated with or without 10 μM Oligomycin and 4 μM antimycin for 4 h. Cells were incubated with 100 nM MitoTracker™ Deep Red (Thermo, M22426) FM in full media at 37 °C for 15 minutes and transferred to a prewarmed microscope stage after washing with dye-free media. Fluorescent images were obtained using a Zeiss 900 LSM microscope with a Plan-apochromat 63 x lens with a 1.4 NA and oil immersion. Analysis was carried out using ImageJ Fiji.

Image 3D Rendering

The image stacks acquired from confocal microscopy as described above were processed using Imaris Bitplane 10.1 software (Oxford Instruments) to generate 3D reconstructions. The Imaris 'surface' feature was used to create the 3D reconstructions of each channel based on local intensities.

Renal Ischemia Reperfusion Injury Model

A bilateral renal ischemia-reperfusion injury (r-IRI) model was established using a standard surgical technique. The mice were anesthetized through inhalation of isoflurane. Two back incisions were made to expose the kidneys, after which bilateral renal ischemia was induced by clamping both renal pedicles for 30 minutes. The kidneys were identified as ischemic based on a visual assessment, noting a change in color from pink to dark red. Following the release of the clamps, reperfusion was confirmed visually when the kidneys returned to a normal pink color. The sham mice underwent the same surgical procedure without renal pedicles clamped.

Kidney Histological and Functional Assessment

Seventy-two hours following the ischemic period, the mice were euthanized, and blood samples were collected through cardiac puncture. Serum was then separated for the analysis of creatinine (CREA) and blood urea nitrogen (BUN) levels (Roche Diagnostics). Both kidneys were harvested and fixed in 4% paraformaldehyde for histological analysis, which included H&E staining and PAS staining, performed according to the manufacturers' protocols. For histological evaluation, the percentage of damaged tubules in the cortical fields was calculated for each kidney. Tubular injury was characterized by tubular dilation, atrophy, the presence of casts, vacuolization, degeneration, and the detachment of tubular epithelial cells, as well as the loss of the brush border and thickening of the tubular basement membrane. At least ten randomly

selected, non-overlapping fields were analyzed to determine the average number of damaged tubules. The assessment of tubular injury was categorized using a scoring system as previously described[81]: 0 indicated no injury; 1 represented 1-10% injured tubules; 2 indicated 11-25% injured tubules; 3 denoted 26-50% injured tubules; 4 signified 51-74% injured tubules; and 5 indicated 75% or more injured tubules.

Focal Cerebral Ischemia Model

All surgeries were performed under aseptic conditions by a single experienced animal surgeon. Transient acute focal cerebral ischemia was induced using reversible intraluminal middle cerebral artery occlusion (MCAO), following previously established protocols[82]. Male mice were anesthetized with isoflurane. A 2 cm incision was made in the center of the anterior neck. Left unilateral MCAO was achieved by inserting a silicon rubber-coated nylon monofilament (RWD Life Science, Co., Ltd., Shenzhen, Guangdong, China) into the internal carotid artery through the external carotid artery. The filament was advanced 9 to 10 mm past the carotid bifurcation until slight resistance was encountered or the marking point reached the bifurcation. The effectiveness of the MCAO was verified by monitoring cortical blood flow with a Laser Speckle Contrast Imaging System (RFLSI ZW, RWD Life Science, Co., Ltd., Shenzhen, Guangdong, China). Animals were excluded from the study if the mean ipsilateral laser speckle signal exceeded 30% of the baseline recorded in the pre-ischemic ipsilateral hemisphere. To maintain body temperature during the MCAO procedure, a heating pad was used, keeping it at 36.5 ± 0.5 °C. After 60 minutes of occlusion, the filament was retracted to allow reperfusion, and the incision was closed with 4-0 surgical sutures (JINHUAN, Co., LTD). In sham-operated animals, the occluding filament was inserted only 5 mm above the carotid bifurcation. The surgeon remained blinded to the different experimental groups.

Adeno-associated Viral Vectors Production and Stereotaxic Injection

To restore the expression of *Smcr8* in the brains of *Smcr8* cKO mice, the DNA sequences of human $SMCR8^{WT}$ and $SMCR8^{S471A}$ were cloned into the pssAAV-CB-EGFP vector. The constructed plasmids were then packaged into AAV-PHP.eB capsids, employing the triple-plasmid transfection method, and subsequently purified by two rounds of cesium chloride ultracentrifugation as previously described[83]. The genome titer and purity of the rAAV vectors were evaluated by qPCR and silver staining (Pierce silver stain kit). The viral vectors were aliquoted and stored at -80°C before use.

All surgeries were performed under aseptic conditions. Recombinant adeno-associated virus (rAAV) injections into specific brain regions were conducted using a stereotaxic instrument (World Precision Instruments). For each mouse, 4×10^{10} GC of ssAAV8-$SMCR8^{S471A}$ or 4×10^{10} of ssAAV8-$SMCR8^{WT}$ were injected into the CA3 region of the left hippocampus (coordinates: Bregma: -2 mm, lateral: 2 mm, depth: 2 mm). In contrast, control mice received 4×10^{10} injections of ssAAV8-eGFP. After the injection, the needle was left in place for 5 minutes before being withdrawn at a rate of 1 mm/min. Proper postoperative care was provided until the animals had fully recovered. At 35 days post-injection, focal cerebral ischemia was induced in the mice through MCAO and subsequent reperfusion. Neurological assessments and infarct volume measurements were conducted 24 hours after reperfusion.

Neurological Assessment

The neurological assessment following surgery was conducted by an investigator who was blinded to the experimental groups, and the results were subsequently confirmed by a second investigator, also blinded to the experimental groups. The neurological deficits of each mouse were evaluated at 24 hours post-MCAO/reperfusion using a Modified Neurological Severity Score (mNSS) system.

Rotarod Test

The motor coordination of the mice post-surgery was assessed using a rotarod treadmill designed for mice operating in the accelerating rotor mode. This mode consisted of 10 speed settings ranging from 4 to 40 rpm over a span of 5 minutes. The time taken for the animal to remain on the rod before falling off was noted as the retention time. Mice that stayed on the accelerating rod for a full 300 seconds were classified as survivors. Prior to the surgery, the animals underwent a training period of 2 days, with 3 trials conducted each day, during which their average duration on the rod was recorded to establish stable baseline values. The performance on the rotarod test was evaluated three times one day after the ischemic event.

Grip Strength Test

A Grip Strength Meter was utilized to assess the grip strength of the forelimbs in mice. Prior to conducting the grip strength test, the mice were weighed. As each mouse grasped the bar, the maximum pull force, measured in grams, was captured using a digital force transducer. The grip strength results were shown as the ratio of grip force to body weight (g).

Infarct Volume Analysis

After 24 hours of reperfusion, the mice were euthanized, and their brains were quickly extracted and stored at -20°C for 20 minutes. Coronal slices were prepared at 2 mm intervals from the frontal poles. These 2 mm brain sections were then incubated in a 1% solution of 2,3,5-triphenyl tetrazolium chloride (TTC, Sigma-Aldrich) in phosphate-buffered saline (PBS) for 15 minutes at 37°C, followed by fixation in 10% formalin for 24 hours. Infarct volume was quantified using digital imaging, and the images were analyzed with Image J software. A blinded operator measured the areas of infarction (unstained, white), the ipsilateral hemisphere (unstained, white, plus stained red brick), and the contralateral hemisphere (stained red brick) for each section.

Hematoxylin & Eosin Staining and Nissl Staining

Brain tissue samples were collected and fixed in 4% paraformaldehyde at 4 °C for 24 hours. The samples were then embedded in paraffin and sectioned at a thickness of 5 μm. The sections were then incubated in hematoxylin solution, followed by eosin solution (Sigma-Aldrich). For Nissl staining, the sections were incubated in a 0.1% thionin solution (Sigma-Aldrich). The slides were then differentiated in a 95% ethanol solution.

Transmission Electron Microscopy (TEM)

Brain tissues were fixed via transcardiac perfusion, initially with saline, followed by a buffered solution at pH 7.2-7.4 containing 2.5% glutaraldehyde for a duration of 7 days, and cells were fixed by 2.5% glutaraldehyde for 12 h. This was followed by a secondary fixation utilizing 1% osmium tetroxide for 1 hour. After fixation, the samples were rinsed with phosphate-buffered saline (PBS) and subsequently dehydrated through a series of ethanol solutions: 30% ethanol for 10 minutes, 50% ethanol for 10 minutes, 70% ethanol for 10 minutes, 90% ethanol for 10 minutes, and 100% ethanol for two intervals of 10 minutes each. The samples were then infiltrated with propylene oxide for two additional intervals of 10 minutes. Following dehydration, the samples were embedded in epoxy resin. Ultra-thin sections, 60-100 nm in thickness, were prepared using an ARTOS 3D microtome (Leica) and stained with uranyl acetate and lead citrate prior to transmission electron microscopy (TEM) examination. Imaging was performed using a JEM-2100plus microscope (JEOL) at 120 kV.

Statistical Analysis

All experiments were independently repeated at least three times. Data are presented as mean ± SD (or mean ± SEM, as indicated) or as median with interquartile range. Normality was assessed using normality and lognormality tests. For comparisons among multiple groups, one-way ANOVA followed by Tukey's multiple-comparisons test was used for parametric data, and the Kruskal–Wallis test followed by Dunn's multiple-comparisons test was used for nonparametric data. For comparisons between two groups, two-tailed Student's t-test (parametric) or the Mann–Whitney test (nonparametric) was used. Statistical analyses were performed using GraphPad Prism 8. $P < 0.05$ was considered statistically significant.

Reference

1. Collaborators, G.B.D.L.R.o.S. *et al.* Global, Regional, and Country-Specific Lifetime Risks of Stroke, 1990 and 2016. *N Engl J Med* **379**, 2429-2437 (2018).
2. Diseases, G.B.D. & Injuries, C. Global burden of 369 diseases and injuries in 204 countries and territories, 1990-2019: a systematic analysis for the Global Burden of Disease Study 2019. *Lancet* **396**, 1204-1222 (2020).
3. Virani, S.S. *et al.* Heart Disease and Stroke Statistics-2021 Update: A Report From the American Heart Association. *Circulation* **143**, e254-e743 (2021).
4. Collaborators, G.B.D.S.R.F. Global, regional, and national burden of stroke and its risk factors, 1990-2021: a systematic analysis for the Global Burden of Disease Study 2021. *Lancet Neurol* **23**, 973-1003 (2024).
5. Francis, A. *et al.* Chronic kidney disease and the global public health agenda: an international consensus. *Nat Rev Nephrol* **20**, 473-485 (2024).
6. Sun, J. *et al.* Mitochondria in Sepsis-Induced AKI. *J Am Soc Nephrol* **30**, 1151-1161 (2019).
7. Granger, D.N. & Kvietys, P.R. Reperfusion injury and reactive oxygen species: The evolution of a concept. *Redox Biol* **6**, 524-551 (2015).

8. Chouchani, E.T. *et al.* Ischaemic accumulation of succinate controls reperfusion injury through mitochondrial ROS. *Nature* **515**, 431-435 (2014).
9. Brookes, P.S., Yoon, Y., Robotham, J.L., Anders, M.W. & Sheu, S.S. Calcium, ATP, and ROS: a mitochondrial love-hate triangle. *Am J Physiol Cell Physiol* **287**, C817-833 (2004).
10. Lesnefsky, E.J., Moghaddas, S., Tandler, B., Kerner, J. & Hoppel, C.L. Mitochondrial dysfunction in cardiac disease: ischemia--reperfusion, aging, and heart failure. *J Mol Cell Cardiol* **33**, 1065-1089 (2001).
11. Ramachandra, C.J.A., Hernandez-Resendiz, S., Crespo-Avilan, G.E., Lin, Y.H. & Hausenloy, D.J. Mitochondria in acute myocardial infarction and cardioprotection. *EBioMedicine* **57**, 102884 (2020).
12. Yao, C. *et al.* Mitochondrial dysfunction in acute kidney injury. *Ren Fail* **46**, 2393262 (2024).
13. Vargas, J.N.S., Hamasaki, M., Kawabata, T., Youle, R.J. & Yoshimori, T. The mechanisms and roles of selective autophagy in mammals. *Nat Rev Mol Cell Biol* **24**, 167-185 (2023).
14. Wang, S. *et al.* The mitophagy pathway and its implications in human diseases. *Signal Transduct Target Ther* **8**, 304 (2023).
15. Zhang, L., Dai, L. & Li, D. Mitophagy in neurological disorders. *J Neuroinflammation* **18**, 297 (2021).
16. Baek, S.H. *et al.* Modulation of mitochondrial function and autophagy mediates carnosine neuroprotection against ischemic brain damage. *Stroke* **45**, 2438-2443 (2014).
17. Antico, O., Thompson, P.W., Hertz, N.T., Muqit, M.M.K. & Parton, L.E. Targeting mitophagy in neurodegenerative diseases. *Nat Rev Drug Discov* (2025).
18. Denk, D. *et al.* Effect of the mitophagy inducer urolithin A on age-related immune decline: a randomized, placebo-controlled trial. *Nat Aging* **5**, 2309-2322 (2025).
19. Qader, M.A. *et al.* A systematic review of the therapeutic potential of nicotinamide adenine dinucleotide precursors for cognitive diseases in preclinical rodent models. *BMC Neurosci* **26**, 17 (2025).
20. DeJesus-Hernandez, M. *et al.* Expanded GGGGCC hexanucleotide repeat in noncoding region of C9ORF72 causes chromosome 9p-linked FTD and ALS. *Neuron* **72**, 245-256 (2011).
21. Renton, A.E. *et al.* A hexanucleotide repeat expansion in C9ORF72 is the cause of chromosome 9p21-linked ALS-FTD. *Neuron* **72**, 257-268 (2011).
22. Pang, W. & Hu, F. Cellular and physiological functions of C9ORF72 and implications for ALS/FTD. *J Neurochem* **157**, 334-350 (2021).
23. Mizielinska, S. *et al.* Amyotrophic lateral sclerosis caused by hexanucleotide repeat expansions in C9orf72: from genetics to therapeutics. *Lancet Neurol* **24**, 261-274 (2025).
24. Jiang, L., Zhang, T., Lu, K. & Qi, S. The progress in C9orf72 research: ALS/FTD pathogenesis, functions and structure. *Small GTPases* **13**, 56-76 (2022).
25. Lan, Y., Sullivan, P.M. & Hu, F. SMCR8 negatively regulates AKT and MTORC1 signaling to modulate lysosome biogenesis and tissue homeostasis. *Autophagy* **15**, 871-885 (2019).
26. Zhang, Y. *et al.* The C9orf72-interacting protein Smcr8 is a negative regulator of autoimmunity and lysosomal exocytosis. *Genes Dev* **32**, 929-943 (2018).
27. Yang, M. *et al.* A C9ORF72/SMCR8-containing complex regulates ULK1 and plays a dual role in autophagy. *Sci Adv* **2**, e1601167 (2016).

28. Sullivan, P.M. *et al.* The ALS/FTLD associated protein C9orf72 associates with SMCR8 and WDR41 to regulate the autophagy-lysosome pathway. *Acta Neuropathol Commun* **4**, 51 (2016).
29. Ugolino, J. *et al.* Loss of C9orf72 Enhances Autophagic Activity via Deregulated mTOR and TFEB Signaling. *PLoS Genet* **12**, e1006443 (2016).
30. Zucha, D. *et al.* Spatiotemporal transcriptomic map of glial cell response in a mouse model of acute brain ischemia. *Proc Natl Acad Sci U S A* **121**, e2404203121 (2024).
31. Bormann, D. *et al.* Single-nucleus RNA sequencing reveals glial cell type-specific responses to ischemic stroke in male rodents. *Nat Commun* **15**, 6232 (2024).
32. Cui, M. *et al.* Dynamic Transcriptional Responses to Injury of Regenerative and Non-regenerative Cardiomyocytes Revealed by Single-Nucleus RNA Sequencing. *Dev Cell* **53**, 102-116 e108 (2020).
33. Balzer, M.S. *et al.* Single-cell analysis highlights differences in druggable pathways underlying adaptive or fibrotic kidney regeneration. *Nat Commun* **13**, 4018 (2022).
34. Malone, A.F. *et al.* Harnessing Expressed Single Nucleotide Variation and Single Cell RNA Sequencing To Define Immune Cell Chimerism in the Rejecting Kidney Transplant. *J Am Soc Nephrol* **31**, 1977-1986 (2020).
35. Xu, X. *et al.* Tet2 acts in the lateral habenula to regulate social preference in mice. *Cell Rep* **42**, 112695 (2023).
36. Zhang, Y. *et al.* HDAC9-mediated epithelial cell cycle arrest in G2/M contributes to kidney fibrosis in male mice. *Nat Commun* **14**, 3007 (2023).
37. Tang, D. *et al.* ALS-linked C9orf72-SMCR8 complex is a negative regulator of primary ciliogenesis. *Proc Natl Acad Sci U S A* **120**, e2220496120 (2023).
38. Tang, D. *et al.* Cryo-EM structure of C9ORF72-SMCR8-WDR41 reveals the role as a GAP for Rab8a and Rab11a. *Proc Natl Acad Sci U S A* **117**, 9876-9883 (2020).
39. Wang, C. A Sensitive and Quantitative mKeima Assay for Mitophagy via FACS. *Curr Protoc Cell Biol* **86**, e99 (2020).
40. Jung, J. *et al.* Multiplex image-based autophagy RNAi screening identifies SMCR8 as ULK1 kinase activity and gene expression regulator. *Elife* **6** (2017).
41. Zhang, M. *et al.* Mechanistic insights into the interactions of TAX1BP1 with RB1CC1 and mammalian ATG8 family proteins. *Proceedings of the National Academy of Sciences* **121**, e2315550121 (2024).
42. Eickhorst, C. *et al.* FIP200 Phosphorylation Regulates Late Steps in Mitophagy. *J Mol Biol*, 168631 (2024).
43. Wu, S. *et al.* Structural basis for TNIP1 binding to FIP200 during mitophagy. *J Biol Chem* **300**, 107605 (2024).
44. Zheng, Q. *et al.* Calcium transients on the ER surface trigger liquid-liquid phase separation of FIP200 to specify autophagosome initiation sites. *Cell* **185**, 4082-4098 e4022 (2022).
45. Turco, E. *et al.* FIP200 Claw Domain Binding to p62 Promotes Autophagosome Formation at Ubiquitin Condensates. *Mol Cell* **74**, 330-346 e311 (2019).
46. Zhou, Z. *et al.* Phosphorylation regulates the binding of autophagy receptors to FIP200 Claw domain for selective autophagy initiation. *Nat Commun* **12**, 1570 (2021).

47. Sellier, C. *et al.* Loss of C9ORF72 impairs autophagy and synergizes with polyQ Ataxin-2 to induce motor neuron dysfunction and cell death. *EMBO J* **35**, 1276-1297 (2016).
48. Majounie, E. *et al.* Frequency of the C9orf72 hexanucleotide repeat expansion in patients with amyotrophic lateral sclerosis and frontotemporal dementia: a cross-sectional study. *Lancet Neurol* **11**, 323-330 (2012).
49. Webster, C.P. *et al.* The C9orf72 protein interacts with Rab1a and the ULK1 complex to regulate initiation of autophagy. *EMBO J* **35**, 1656-1676 (2016).
50. Tang, D., Bao, H. & Qi, S. The C9orf72-SMCR8 complex suppresses primary ciliogenesis as a RAB8A GAP. *Autophagy* **20**, 1205-1207 (2024).
51. Zhang, S. *et al.* C9orf72-catalyzed GTP loading of Rab39A enables HOPS-mediated membrane tethering and fusion in mammalian autophagy. *Nat Commun* **14**, 6360 (2023).
52. Su, M.Y., Fromm, S.A., Zoncu, R. & Hurley, J.H. Structure of the C9orf72 ARF GAP complex that is haploinsufficient in ALS and FTD. *Nature* **585**, 251-255 (2020).
53. Tang, D. *et al.* Cryo-EM structure of C9ORF72–SMCR8–WDR41 reveals the role as a GAP for Rab8a and Rab11a. *Proceedings of the National Academy of Sciences* **117**, 9876-9883 (2020).
54. Licheva, M. *et al.* Phase separation of initiation hubs on cargo is a trigger switch for selective autophagy. *Nat Cell Biol* (2025).
55. Shi, X. *et al.* ULK complex organization in autophagy by a C-shaped FIP200 N-terminal domain dimer. *J Cell Biol* **219** (2020).
56. Jung, J. & Behrends, C. Multifaceted role of SMCR8 as autophagy regulator. *Small GTPases* **11**, 53-61 (2020).
57. Vargas, J.N.S. *et al.* Spatiotemporal Control of ULK1 Activation by NDP52 and TBK1 during Selective Autophagy. *Mol Cell* **74**, 347-362 e346 (2019).
58. Tang, D., Sheng, J., Xu, L., Yan, C. & Qi, S. The C9orf72-SMCR8-WDR41 complex is a GAP for small GTPases. *Autophagy* **16**, 1542-1543 (2020).
59. Goodier, J.L. *et al.* C9orf72-associated SMCR8 protein binds in the ubiquitin pathway and with proteins linked with neurological disease. *Acta Neuropathol Commun* **8**, 110 (2020).
60. Amick, J., Tharkeshwar, A.K., Talaia, G. & Ferguson, S.M. PQLC2 recruits the C9orf72 complex to lysosomes in response to cationic amino acid starvation. *J Cell Biol* **219** (2020).
61. Talaia, G., Amick, J. & Ferguson, S.M. Receptor-like role for PQLC2 amino acid transporter in the lysosomal sensing of cationic amino acids. *bioRxiv* (2020).
62. Zhu, Q. *et al.* Reduced C9ORF72 function exacerbates gain of toxicity from ALS/FTD-causing repeat expansion in C9orf72. *Nat Neurosci* **23**, 615-624 (2020).
63. Butti, Z., Pan, Y.E., Giacomotto, J. & Patten, S.A. Reduced C9orf72 function leads to defective synaptic vesicle release and neuromuscular dysfunction in zebrafish. *Commun Biol* **4**, 792 (2021).
64. Hao, Y. *et al.* Integrated analysis of multimodal single-cell data. *Cell* **184**, 3573-3587 e3529 (2021).
65. Yan, L., Edn. 0.1.19 An easy-to-use way to draw pretty Venn diagrams using 'ggplot2'. This package provides functions to create Venn diagrams with customizable colors, labels, and styling options. (2025).

66. Gene Ontology, C. The Gene Ontology resource: enriching a GOld mine. *Nucleic Acids Res* **49**, D325-D334 (2021).
67. Ashburner, M. *et al.* Gene ontology: tool for the unification of biology. The Gene Ontology Consortium. *Nat Genet* **25**, 25-29 (2000).
68. Kanehisa, M. & Goto, S. KEGG: kyoto encyclopedia of genes and genomes. *Nucleic Acids Res* **28**, 27-30 (2000).
69. Kanehisa, M., Furumichi, M., Sato, Y., Matsuura, Y. & Ishiguro-Watanabe, M. KEGG: biological systems database as a model of the real world. *Nucleic Acids Res* **53**, D672-D677 (2025).
70. Wu, T. *et al.* clusterProfiler 4.0: A universal enrichment tool for interpreting omics data. *Innovation (Camb)* **2**, 100141 (2021).
71. Benjamini, Y. & Hochberg, Y. Controlling the False Discovery Rate: A Practical and Powerful Approach to Multiple Testing. *Journal of the Royal Statistical Society: Series B (Methodological)* **57**, 289-300 (1995).
72. Lazarou, M. *et al.* The ubiquitin kinase PINK1 recruits autophagy receptors to induce mitophagy. *Nature* **524**, 309-314 (2015).
73. Cong, L. *et al.* Multiplex Genome Engineering Using CRISPR/Cas Systems. *Science* **339**, 819-823 (2013).
74. Tai, R.-Z. & Zhao, Z.-T. Overview of SSRF phase-II beamlines. *Nuclear Science and Techniques* **35**, 137 (2024).
75. Otwinowski, Z. & Minor, W. Processing of X-ray diffraction data collected in oscillation mode. *Methods Enzymol* **276**, 307-326 (1997).
76. Emsley, P. & Cowtan, K. Coot: model-building tools for molecular graphics. *Acta Crystallogr D Biol Crystallogr* **60**, 2126-2132 (2004).
77. Liebschner, D. *et al.* Macromolecular structure determination using X-rays, neutrons and electrons: recent developments in Phenix. *Acta Crystallogr D Struct Biol* **75**, 861-877 (2019).
78. Schrodinger, LLC (2015).
79. Jin, X. *et al.* Membraneless organelles formed by liquid-liquid phase separation increase bacterial fitness. *Sci Adv* **7**, eabh2929 (2021).
80. Muzzopappa, F. *et al.* Detecting and quantifying liquid-liquid phase separation in living cells by model-free calibrated half-bleaching. *Nat Commun* **13**, 7787 (2022).
81. Takaori, K. *et al.* Severity and Frequency of Proximal Tubule Injury Determines Renal Prognosis. *J Am Soc Nephrol* **27**, 2393-2406 (2016).
82. Chiang, T., Messing, R.O. & Chou, W.H. Mouse model of middle cerebral artery occlusion. *J Vis Exp* (2011).
83. Wang, Q. *et al.* Efficient production of dual recombinant adeno-associated viral vectors for factor VIII delivery. *Hum Gene Ther Methods* **25**, 261-268 (2014).

Acknowledgments: We thank Dr. Changxin Ma, Prof. Tongjin Zhao (Fudan University), Prof. Du Feng (Guangzhou Medical University), Prof. Liang Ge (Tsinghua University), and Prof. Xingguo Liu (GIBH, CAS) for their constructive suggestions. We also appreciate Bo Su and Jinsai Wu at the Histology and Imaging Platform, Core Facilities of West China Hospital, Sichuan University, for their technical support. We thank the staff at Tianfu Jincheng laboratory

Cryo-EM center for their technical support. We thank Xinyuan Wang and Yi Zhong from the Proteomics-Metabolomics Platform of West China Hospital for their assistance with proteomics analyses. We acknowledge the staff at BL10U2 of at the Shanghai Synchrotron Radiation Facility (SSRF), and BL18U1, BL19U1 of the National Facility for Protein Science in Shanghai, Zhangjiang Laboratory (NFPS, ZJLab), for their support in data collection.

Funding: This work was supported by the NSFC grants 32470738(S.Q.), 32071214 (S.Q.), 32471311 (D.T.), 32201025 (D.T.), U25A20745(Z.L.), 32471507 (Z.L.), 32170648 (H.C.), and 82304600 (S.F.), Sichuan Science and Technology Program 2026NSFSCZY0111 (S.Q.), 2024NSFSC1495 (S.F.), and West China Hospital grant ZYYC23012 (S.Q.).

Author contributions: Q.S. initiated the project. T.D., B.H., F.S., Chen.W., Z.H, X.L, J.X., C.J., L.Z., and Q.S. designed and performed the biochemical and cell biological analysis. Z.X., T.D., D.L., and Q.S. designed and performed the LC-MS/MS analysis. T.D., B.H., H.X., Cheng.W., and Q.S. performed the structural analysis. Chen.W., T.D., B.H., S.L., T.X., and Q.S. designed and performed the imaging analysis and FRAP analysis. B.H., T.D., L.Z., and Q.S. designed and performed FACS analysis. T.D., F.S., S.Q., and Q.S. designed and performed TEM analysis. F.S., T.D., Z.H., D.B., W.K., and Q.S. designed and performed the analysis of ischemia injury animal models. L.Y., T.D., F.S., X.L., G.L., B.D., and Q.S. designed and generated AAV vectors. Ci.H., Cai.H., F.S., T.D., and Q.S. designed and performed RNA-seq data analysis. Q.S., T.D., F.S., L.Z., Cai H., L.Z., and G.L. wrote the manuscript. All the authors participated in the project, discussed the results, wrote the methods parts, and commented on the manuscript.

Competing interests: B.D. is a founder and the president of Sichuan Real & Best Biotech Co., Ltd.

Data availability: Coordinates and structure factor of the structure reported here have been deposited into the Protein Data Bank with PDB Code: 9LUA.This paper does not report original code. The RNA-seq data used in this study were obtained from a previously published study and are publicly available in the NCBI Gene Expression Omnibus (GEO) under the acession numbers GSE233815, GSE180420, GSE130699, GSE250245, and GSE145927.

Supplementary Materials

Figs. S1 to S10 and Table S1 to S4

Figure legends

Figure 1. *C9ORF72* is transiently induced by ischemic stress and defines a protective response *in vivo*

a. Intersection of significantly upregulated genes (DEGs) across multiple IRI transcriptomic datasets, identifying *C9ORF72* as a conserved ischemia-responsive gene (Bonferroni-adjusted $P < 0.0001$ and $\log_2$ FC > 0.2).

b. Volcano plot of DEGs in ischemic mouse brain relative to sham controls (Bonferroni-

adjusted $P < 0.01$, $|\log_2 FC| > 0.5$).

c,d. *C9orf72* expression in sham and ischemic mouse brain tissues (c) and human kidney transplant samples (d), suggesting conserved induction during IRI.

e. Experiment workflow for renal and cerebral IRI models.

f,g. Renal function assessed by serum creatinine (CREA) (f) and blood urea nitrogen (BUN) (g) in WT and *C9orf72* cKO mice subjected to sham or r-IRI surgery.

h,i. Representative H&E and PAS-stained kidney sections (h) and semiquantitative tubular injury scores (i) showing exacerbated renal damage in *C9orf72* cKO mice after r-IRI. Scale bar: 50 μm.

j-l. Modified neurological severity score (mNSS) assessment (j), grip strength test (k), and rotarod test (l) in WT or *C9orf72* cKO mice following MCAO.

m,n. Representative TTC-stained brain sections (m) and quantification of infarct volume (n).

o. Representative H&E staining (Hippocampus and Cortex,) and Nissl staining of brain sections showing increased neuronal loss in *C9orf72* cKO mice. Scale bar: 50 μm

p. TEM images revealing increased mitochondrial damage in ischemic brains of *C9orf72* cKO mice. White arrows: intact mitochondria; red arrows: damaged mitochondria. Scale bar: 2 μm.

q. KEGG pathway enrichment analysis highlighting consistent induction of autophagy- and mitophagy-related pathways across IRI datasets.

Values: mean ± SEM, n>6 IRI mice (f, g, i, j, k, l, and n). Significance: two-sided Welch's t-test (c, d); ordinary one-way ANOVA, Tukey's multiple comparisons test (f, g, i, j, k, l, and n); Benjamini–Hochberg-adjusted *P*-values (q).

Figure 2. SMCR8 functions as the effector module linking the CS complex to mitophagy

a. Immunoblot analysis of C9ORF72 and SMCR8 protein levels in WT, *C9ORF72* KO and *SMCR8* KO HeLa cells.

b. Validation of C9ORF72, SMCR8 and Parkin protein levels in *C9ORF72-SMCR8* double knockout (DKO) HeLa cells expressing mKeima and Flag-Parkin.

c,d. FACS analysis (c) and quantification (d) of mitophagic flux in DKO HeLa cells transfected with GFP, GFP-C9ORF72 or GFP-SMCR8, and treated with or without O/A for 4 h.

e,f. TEM analysis (e) and quantification (f) of mitochondria-containing vesicles in WT and *SMCR8* shRNA knock down (KD) HeLa cells stably expressing Flag-Parkin treated with BafA1 for 2 h followed by O/A+BafA1 treatment for 1 h. Pink arrows: mitochondria-containing vesicles. Scale bar: 1 μm.

g-j. Renal function (g, h), histopathology (i), and tubular injury scores (j) in WT and *Smcr8* cKO mice following r-IRI. Scale bar: 50 μm.

k-p. Neurological performance (k-m), infarct volume (n, o), and neuronal integrity (p) in WT and *Smcr8* cKO mice after MCAO. Scale bar: 50 μm

q. TEM analysis showing aggravated mitochondrial damage in *Smcr8*-deficient ischemic brain tissue. White arrows: intact mitochondria; red arrows: damaged mitochondria. Scale bar: 2 μm.

Values: mean ± SD, n=3 independent experiments (d); median ± interquartile range, n=3 independent experiments with 10 random fields (f); mean ± SEM, n>6 IRI mice (g, h, j, and o) and n>8 IRI mice (k, l, and m). Significance: ordinary one-way ANOVA, Tukey's multiple comparisons test (d, g, h, j, k, l, m, and o); Mann-Whitney test (f).

Figure 3. SMCR8 engages FIP200 to license condensate during mitophagy

a. Schematic of domain organization and interactions between the C9ORF72-SMCR8 complex and the ULK1 complex.

b. Co-IP analysis demonstrating selective interaction of SMCR8, but not C9ORF72, with endogenous FIP200 across genetic backgrounds.

c,d. FRAP analysis (c) and quantification (d) of GFP-FIP200 puncta dynamics in *C9ORF72-SMCR8* double knockout (DKO) COS7 cells transfected with GFP-FIP200 and mCherry-SMCR8 or mCherry-C9ORF72, and then treated with O/A for 1 h. Scale bar: 2 μm.

e. Confocal imaging and line-scan analysis showing enrichment of SMCR8 within FIP200 condensates upon mitophagy induction. Red line: SMCR8, C9ORF72 or SMCR8-C9ORF72; green line: FIP200. Scale bar: 5 μm.

f,g. Quantification of FIP200 puncta area (f) or number (g) in DKO COS7 cells from (e), demonstrating SMCR8-dependent condensate formation.

All values: mean ± SEM, n=3 independent experiments with >10 cells. Significance: Kruskal–Wallis, Dunn's multiple-comparisons test (h); ordinary one-way ANOVA, Tukey's

multiple comparisons test (g).

Figure 4. ULK1 phosphorylation of SMCR8 licenses FIP200 condensate formation and mitophagy

a. Identification of candidate FIR motifs and phosphorylation sites within SMCR8. Pink brick highlights potential phosphorylation sites, while blue brick indicates the most conserved residues among FIR motifs.

b,c. Co-IP analysis (b) and quantification (c) showing Ser471-dependent interaction between SMCR8 and FIP200. GFP-SMCR8, or GFP-SMCR8^{S471A}, or SMCR8^{S516A} was expressed in *SMCR8* KO HEK293T cells. The level of FIP200 was normalized to GFP-SMCR8.

d,e. LC-MS/MS identification (d) and quantification of (e) SMCR8 Ser471 phosphorylation in response to mitochondrial stress. The peptide sequence is shown at the top, with b- and y-type ions labeled (d). Details of phosphorylation sites in SMCR8 are provided in Table S1. Details of the relative log2 median normalized intensity of pho-SMCR8^{S471} between untreated and O/A treated group are provided in Table S2.

f. Structure model of the phosphorylated SMCR8 FIR bound to the FIP200 Claw domain. Black box highlights details of the interface between FIP200 and SMCR8, with key residues and hydrogen bonds labeled. Blue: FIP200 Claw domain; orange: p-SMCR8 FIR; red: pho-Ser471.

g,h. Mutational analysis validating key residues required for SMCR8–FIP200 interaction Co-IP analysis (g) and quantification (h) of the interaction of GFP-FIP200 and endogenous SMCR8 in *FIP200* KO HEK293T cells expressing GFP-FIP200, FIP200^{N1572A} and FIP200^{R1573A}. The levels of SMCR8 were normalized to those of GFP-FIP200 for comparative analysis.

i,j. Pharmacological and genetic evidence identifying ULK1 as the kinase responsible for Ser471 phosphorylation. WB analysis (i) and quantification (j) of SMCR8 phosphorylation at Ser471 in HEK293T cells. GFP-tagged SMCR8 or SMCR8^{S471A} was overexpressed in HEK293T cells as indicated. Post-transfection, cells were treated with 1 μM ULK1 inhibitor MRT68921 or 2 μM TBK1 inhibitor GSK8612. The phosphorylation level of SMCR8 at Ser471 was normalized to the total SMCR8 level.

k. Confocal imaging and line-scan analysis showing Ser471-dependent FIP200 condensate dynamics upon O/A treatment. Red line: SMCR8; green line: FIP200. Scale bar: 5 μm.

l,m. FRAP analysis (l) and quantification (m) of GFP-FIP200 puncta dynamics in DKO COS7 indicating Ser471-dependent FIP200 condensate dynamics. Scale bar: 2 μm.

n,o. Imaris 3D reconstruction (n) and quantification (o) of the overlap volume of mitochondria and GFP-FIP200 puncta in DKO COS7 cells showing Ser471-dependent recruitment of FIP200 to damaged mitochondria. Scale bar: 5 μm.

p,q. TEM analysis (p) and quantification (q) of mitophagy flux in *SMCR8* KD HeLa cells showing Ser471-dependent recruitment of autophagosome to damaged mitochondria. Pink arrows: mitochondria-containing vesicles. Scale bar: 1 μm.

Values: mean ± SD, n=3 independent experiments (c, h, and j); violin plot, n=5 independent experiments (e); mean ± SEM, n=3 independent experiments with >10 cells (l) or >15 cells (o); median ± interquartile range, n=3 independent experiments with 10 random fields (q). Significance: ordinary one-way ANOVA, Tukey's multiple comparisons test (c, h, j, o, and q); two-tailed Student's t test (e).

Figure 5. SMCR8 Ser471 phosphorylation is required for mitophagy-dependent tissue protection *in vivo*

a. Schematic of AAV-mediated rescue strategy in *Smcr8* cKO mice. CB promoter: combination of CMV enhancer and chicken beta-actin promoter; BGH polyA: the bovine growth hormone (BGH) polyadenylation sequence; ITR: inverted terminal repeat.

b-e. Renal function (b, c), histopathology (d), and tubular injury (e) following r-IRI in mice expressing SMCR8 variants. Scale bar: 50 μm.

f-j. Neurological outcomes (f-h) and infarct volume (i-j) following MCAO in mice expressing SMCR8 variants.

k. Images of H&E staining (Hippocampus and Cortex, scale bar: 50 μm), Nissl staining (Cortex, scale bar: 50 μm) and TEM (scale bar: 2 μm) images of brain sections from *Smcr8* cKO mice injected with AAV-SMCR8 variants and followed by MCAO. TEM analysis showing Ser471-dependent preservation of mitochondrial ultrastructure in ischemic brain tissue.

Values: mean ± SEM, n>6 IRI mice (b, c, e, and j) and n>8 IRI mice (f-h). Significance: ordinary one-way ANOVA, Tukey's multiple comparisons test.

Figure 6. A minimal SMCR8 module reconstitutes condensate-coupled mitophagy and tissue protection

a. Quantification of mitophagic flux (Fig. S10a) in *SMCR8* KO cells expressing truncated SMCR8 variants.

b,c. FRAP analysis (b) and quantification (c) of GFP-FIP200 puncta in *SMCR8* KO COS7 cells showing that a 91-residue SMCR8 peptide fully recapitulates FIP200 condensate dynamics. Scale bar: 2 μm.

d,e. Histopathology (d) and tubular injury (e) following r-IRI in mice expressing SMCR8 peptides. Scale bar: 50 μm.

f-h. Cerebral infarct size (f, g) and neuronal preservation (h) following MCAO in mice expressing SMCR8 peptides. Scale bar: 50 μm.

i. Proposed model illustrating the protective role of the stress-sensing C9ORF72-SMCR8 switch in IRI. Under basal conditions, FIP200 remains diffuse and mitophagy is inactive. Acute ischemic stress induces transient upregulation of C9ORF72, which stabilizes SMCR8. In response to mitochondrial damage, ULK1 phosphorylates SMCR8 at Ser471, enabling its binding to the FIP200 Claw domain and triggering phase separation of FIP200 at damaged mitochondria. These condensates spatially nucleate mitophagosome biogenesis, thereby enabling rapid mitochondrial clearance and tissue protection. A minimal, phosphorylatable 91-residue SMCR8 peptide is sufficient to engage this condensate-licensing mechanism and confer protection against ischemic injury *in vivo*.

Values: mean ± SD, n=3 independent experiments (a); mean ± SEM, n=3 independent experiments with >10 cells (c); mean ± SEM, n>6 IRI mice (e, g). Significance: ordinary one-way ANOVA, Tukey's multiple comparisons test.

Supplementary figure legends

Fig. S1. Conserved stress-responsive *C9ORF72* induction and pathway enrichment across IRI models

a-c. *C9orf72* expression in sham and ischemic samples from rat brain (a), mouse kidney (b) and mouse heart (c), demonstrating conserved induction across organs and species during IRI

d. Immunoblot validation of C9orf72 protein levels in kidney and brain from *C9orf72* cKO mice.

e. Schematic illustration of the cerebral IRI model, including middle cerebral artery occlusion (MCAO) and reperfusion (Created with BioRender.com). Mice underwent 1 h MCAO followed by 24 h of reperfusion. MCA: Middle Cerebral Artery; pCOM: Posterior Communicating Artery; PPA: Persistent Proatlantal Artery; ICA: Internal Carotid Artery; ECA: External Carotid Artery; CCA: Common Carotid Artery.

f. Laser speckle flowgraphy of MCAO mice (LSFG) confirming effective arterial occlusion and reperfusion. Left: before MCAO; middle: during MCAO; right: reperfusion after MCAO.

g. Quantitative cortical blood flow changes before, during, and after MCAO confirming effective arterial occlusion and reperfusion.

h. Gene ontology (GO) enrichment analysis highlighting consistent upregulation of autophagy- and oxidative stress-related pathways across ischemic datasets.

Values: mean ± SEM, n>6 IRI mice (g). Significance: two-sided Welch's t-test (a-c); Paired t test (g); Benjamini–Hochberg-adjusted P-values (h).

Fig. S2. Validation of cellular and mouse models used to assess mitophagy and tissue protection

a. Schematic illustrating the pH-sensitive excitation properties of the mitochondrial-targeted mKeima reporter used to quantify mitophagy.

b. Representative fluorescence images validating mitochondrial localization of mKeima in WT, *SMCR8* KD, *SMCR8* KO, and DKO HeLa cells. Scale bar: 5 μm

c. Immunoblot validation of SMCR8 depletion and Parkin expression in SMCR8 KD cells.

d,e. Flow cytometry analysis (d) and quantification (e) showing reduced O/A-induced mitophagy upon SMCR8 depletion. Cells were treated with or without O/A for 4h.

f,g. Immunoblot analysis (f) and quantification (g) of mitochondrial protein turnover (MFN2, TIM23, TOM20), demonstrating impaired mitophagy in *SMCR8*-deficient cells. The proteins level were normalized against GAPDH.

h. Immunoblot validation of SMCR8 protein loss in kidney and brain tissues from *Smcr8* cKO mice.

i. Experimental workflow for renal and cerebral IRI models.

All values: mean ± SD, n=3 independent experiments. Significance: ordinary one-way ANOVA, Tukey's multiple comparisons test.

Fig. S3. SMCR8 links the CS complex to the ULK1 machinery and regulates FIP200 condensate dynamics

a. Co-IP analysis demonstrating SMCR8-dependent association of the CS complex with the ULK1 complex, requiring FIP200.

b. Co-IP analysis showing selective interaction of the endogenous CS complex with FIP200, but not with other ULK1 components.

c-d. FRAP analysis (c) and quantification (d) showing loss of FIP200 condensate dynamics in DKO COS7 cells. Scale bar: 2 μm.

e-g. Confocal imaging (e) and quantification of FIP200 puncta area (f) and number (g) in WT or DKO COS7 cells, indicating SMCR8-dependent condensate formation.

All values: mean ± SEM, n=3 independent experiments with >10 cells. Significance: Kruskal–Wallis, Dunn's multiple-comparisons test (f); ordinary one-way ANOVA, Tukey's multiple comparisons test (g).

Fig. S4. Mapping the SMCR8-FIP200 Claw interface by truncation and point mutants

a. Co-IP and truncation analysis identifying the FIP200 Claw domain as the exclusive SMCR8-binding region. $FIP200^{NTD}$: residues 1-645; $FIP200^{\Delta NTD}$: residues 636-1594; $FIP200^{\Delta CTD}$: delete residues 1396-1594; $FIP200^{\Delta Claw}$: delete residues 1490-1594; $FIP200^{Claw}$: residues 1404-1594.

b,c. Co-IP (b) and quantification (c) showing that deletion of the SMCR8 Ser471-containing FIR region or mutation of Ser471 disrupts FIP200 binding. The levels of FIP200 were

normalized to those of GFP-SMCR8 for comparative analysis.

All values: mean ± SD, n=3 independent experiments. Significance: ordinary one-way ANOVA, Tukey's multiple comparisons test.

Fig. S5. Structural basis of phosphorylated SMCR8 recognition by the FIP200 Claw domain

a. Gel filtration profile confirming purification of the FIP200 Claw domain. The horizontal axis represents the elution volume, while the vertical axis indicates the ultraviolet (UV) absorption. The UV absorbance is depicted as the blue line. The peak fraction of FIP200 Claw domain from gel filtration was shown by Coomassie blue-stained SDS/PAGE.

b. Overall crystal structure of the FIP200 Claw domain bound to phosphorylated SMCR8 FIR peptide. Blue: FIP200 Claw domains; orange: p-SMCR8.

c. Electron density map validating the position of phosphorylated Ser471. $2F_O$-F_C electron density map of p-SMCR8 is displayed at a contour level of 1.5σ (gray).

d. Detailed view of the hydrogen-bonding network mediating the phosphorylation-dependent SMCR8-FIP200 interaction.

Fig. S6. ULK1 directly phosphorylates SMCR8 at Ser471

a. Immunoprecipitation and LC-MS/MS identifying ULK1 as a kinase associated with SMCR8. The workflow is illustrated on the left. The table on the right summarizes the intensity of SMCR8 and ULK1 (details in Table S4).

b. Quantification of the ULK1 intensity co-immunoprecipitated by GFP-SMCR8 or the GFP-C9ORF72-SMCR8 complex in (a). The levels of ULK1 were normalized to SMCR8 for comparative analysis.

c. *In vitro* kinase and binding assays suggesting that ULK1-mediated phosphorylation of SMCR8 enables direct interaction with the FIP200 Claw domain.

All values: mean ± SD, n=3 independent experiments. Significance: two-tailed Student's t test.

Fig. S7. Ser471 phosphorylation licenses FIP200 condensate formation and dynamics

a,b. Quantification of FIP200 puncta area (a) or number (b) in DKO COS7 cells expressing SMCR8 or SMCR8^{S471A} (Fig. 4k).

c. Confocal imaging showing Ser471-dependent enrichment of SMCR8 within FIP200 condensates in *SMCR8* KO COS7 cells expressing GFP-FIP200 and mCherry-SMCR8 variants. Line-scan profiles show the co-distribution of GFP-FIP200 with mCherry-SMCR8. Red line: SMCR8; green line: FIP200. Scale bar: 5 μm.

d,e. Quantification of the area (d) or number (e) of FIP200 puncta in *SMCR8* KO COS7 cells from (c).

f,g. FRAP analysis (f) and quantification (g) of FIP200 puncta in *SMCR8* KO COS7 cells expressing mCherry-SMCR8 variants suggesting that Ser471 phosphorylation is required for liquid-like dynamics of FIP200 condensates. Scale bar: 2 μm.

All values: mean ± SEM, n=3 independent experiments with >10 cells. Significance: Kruskal–Wallis, Dunn's multiple-comparisons test (a, d); ordinary one-way ANOVA, Tukey's multiple comparisons test (b, e).

Fig. S8. SMCR8 Ser471 phosphorylation is required for mitophagy downstream of ULK1

a-d. FACS analysis and quantification showing that WT SMCR8 or the phospho-mimetic S471E mutant rescues O/A-induced mitophagy in *SMCR8* KO (a, b) and DKO (c, d) cells, whereas FIR deletion or S471A mutation fails.

All values: mean ± SD, n=3 independent experiments. Significance: ordinary one-way ANOVA, Tukey's multiple comparisons test.

Fig. S9. SMCR8 Ser471 phosphorylation couples autophagosome biogenesis to damaged mitochondria

a-f. Confocal imaging and quantification showing Ser471-dependent recruitment of FIP200 to damaged mitochondria. WT, *SMCR8* KO and DKO cells (a, b), DKO (c, d) or *SMCR8* KO (e, f) cells expressing mCherry-SMCR8 variants. FIP200 puncta and mitochondria were indicated with GFP (green) and MitoTracker (magenta), respectively. Relative

quantification of data from (a, c, and e) are shown in (b, d, and f), respectively. Scale bar: 5 μm.

g-l. LC3-mitochondria colocalization analyses showing impaired mitophagosome formation upon disruption of the SMCR8-FIP200 interaction.: WT, *SMCR8* KO, and DKO cells (g, h); *SMCR8* KO (i, j) or DKO (k, l) cells expressing GFP-SMCR8 variants. LC3 puncta and mitochondria were indicated by antibody (green) and MitoTracker (megenta), respectively. Relative quantification of data from (g, i, and k) are shown in (h, j, and i), respectively. Scale bar: 5 μm.

m-p. Imaris 3D reconstruction and quantification of FIP200-mitochondria overlap volume: WT, *SMCR8* KO and DKO cells (m, n) or *SMCR8* KO (o, p) cells expressing mCherry-SMCR8 variants. Relative quantification of data from (m, o) are shown in (n, p), respectively. Scale bar: 5 μm.

Values: mean ± SEM, n=3 independent experiments with>50 cells (b, d, f, h, and j) and >15 cells (n, p). Significance: ordinary one-way ANOVA, Tukey's multiple comparisons test.

Fig. S10. AAV-mediated delivery of a minimal SMCR8 peptide restores mitophagy and supports tissue protection *in vivo*

a. FACS analysis showing that the SMCR8 410-500 peptide rescues mitophagy in *SMCR8* KO HeLa cells in a Ser471-dependent manner. Quantifications are presented in (Fig. 6a).

b. Schematic of preventive AAV-mediated intervention in WT mice.

c,d. Renal function assessment following r-IRI in mice expressing SMCR8 peptide variants.

e-g. Neurological outcomes following MCAO, revealing peptide-mediated protection. mNSS assessment (e), grip strength test (f), and rotarod test (g).

Values: mean ± SEM, n>6 IRI mice (c,d) and n>8 IRI mice (e-g). Significance: ordinary one-way ANOVA, Tukey's multiple comparisons test.

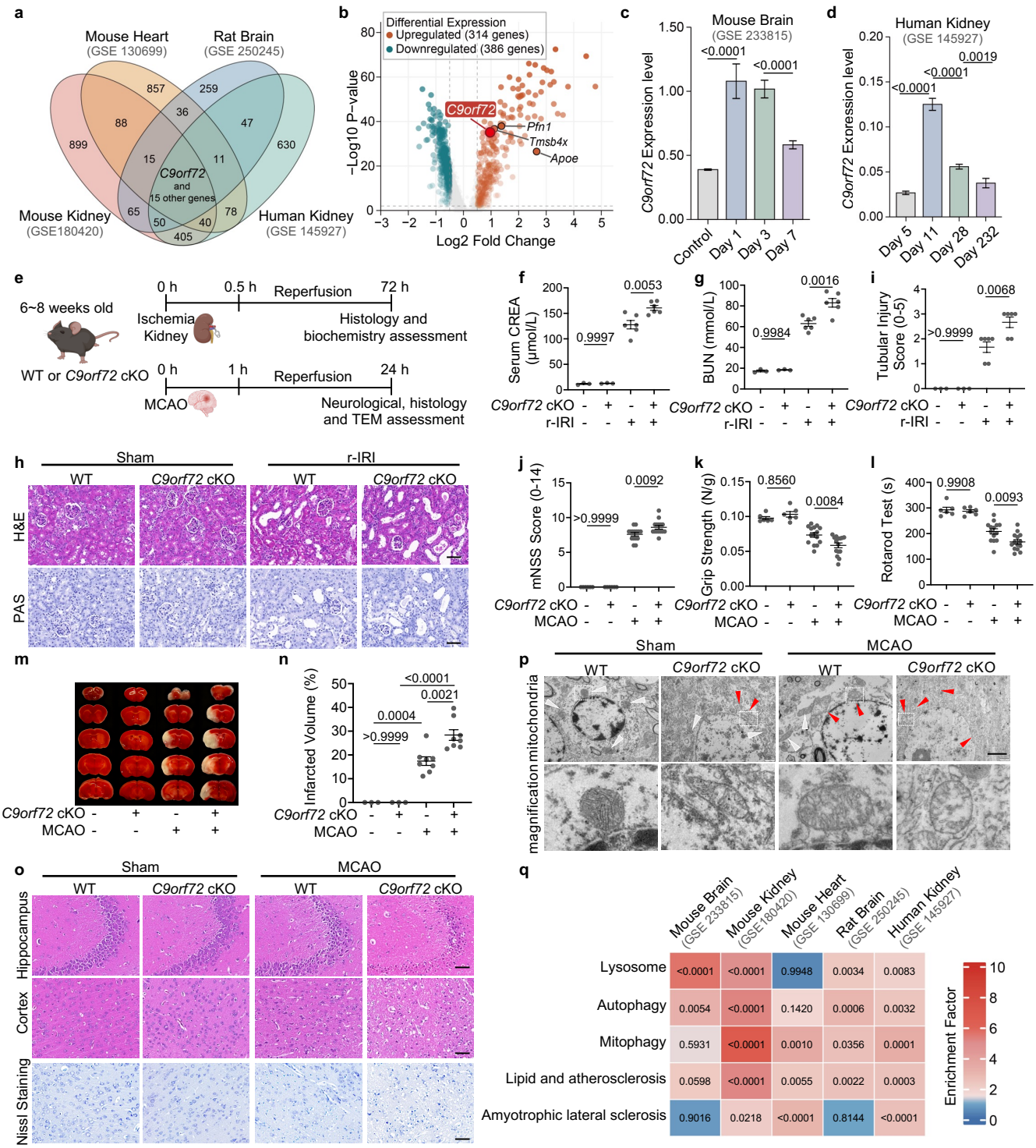
a
Mouse Heart
(GSE 130699)
Rat Brain
(GSE 250245)
Mouse Kidney
(GSE180420)
Human Kidney
(GSE 145927)
C9orf72
and
15 other genes
b
Differential Expression
Upregulated (314 genes)
Downregulated (386 genes)
−Log10 P-value
Log2 Fold Change
C9orf72
Pfn1
Tmsb4x
Apoe
c
Mouse Brain
(GSE 233815)
C9orf72 Expression level
Control
Day 1
Day 3
Day 7
d
Human Kidney
(GSE 145927)
C9orf72 Expression level
Day 5
Day 11
Day 28
Day 232
e
6~8 weeks old
WT or C9orf72 cKO
Ischemia
Kidney
MCAO
Reperfusion
Histology and
biochemistry assessment
Neurological, histology
and TEM assessment
f
Serum CREA
(μmol/L)
g
BUN (mmol/L)
i
Tubular Injury
Score (0-5)
C9orf72 cKO
r-IRI
h
Sham
r-IRI
WT
C9orf72 cKO
H&E
PAS
j
mNSS Score (0-14)
k
Grip Strength (N/g)
l
Rotarod Test (s)
C9orf72 cKO
MCAO
m
n
Infarcted Volume (%)
C9orf72 cKO
MCAO
p
Sham
MCAO
WT
C9orf72 cKO
mitochondria
magnification
o
Sham
MCAO
Hippocampus
Cortex
Nissl Staining
q
Mouse Brain
(GSE 233815)
Mouse Kidney
(GSE180420)
Mouse Heart
(GSE 130699)
Rat Brain
(GSE 250245)
Human Kidney
(GSE 145927)
Lysosome
Autophagy
Mitophagy
Lipid and atherosclerosis
Amyotrophic lateral sclerosis
Enrichment Factor

Figure 1

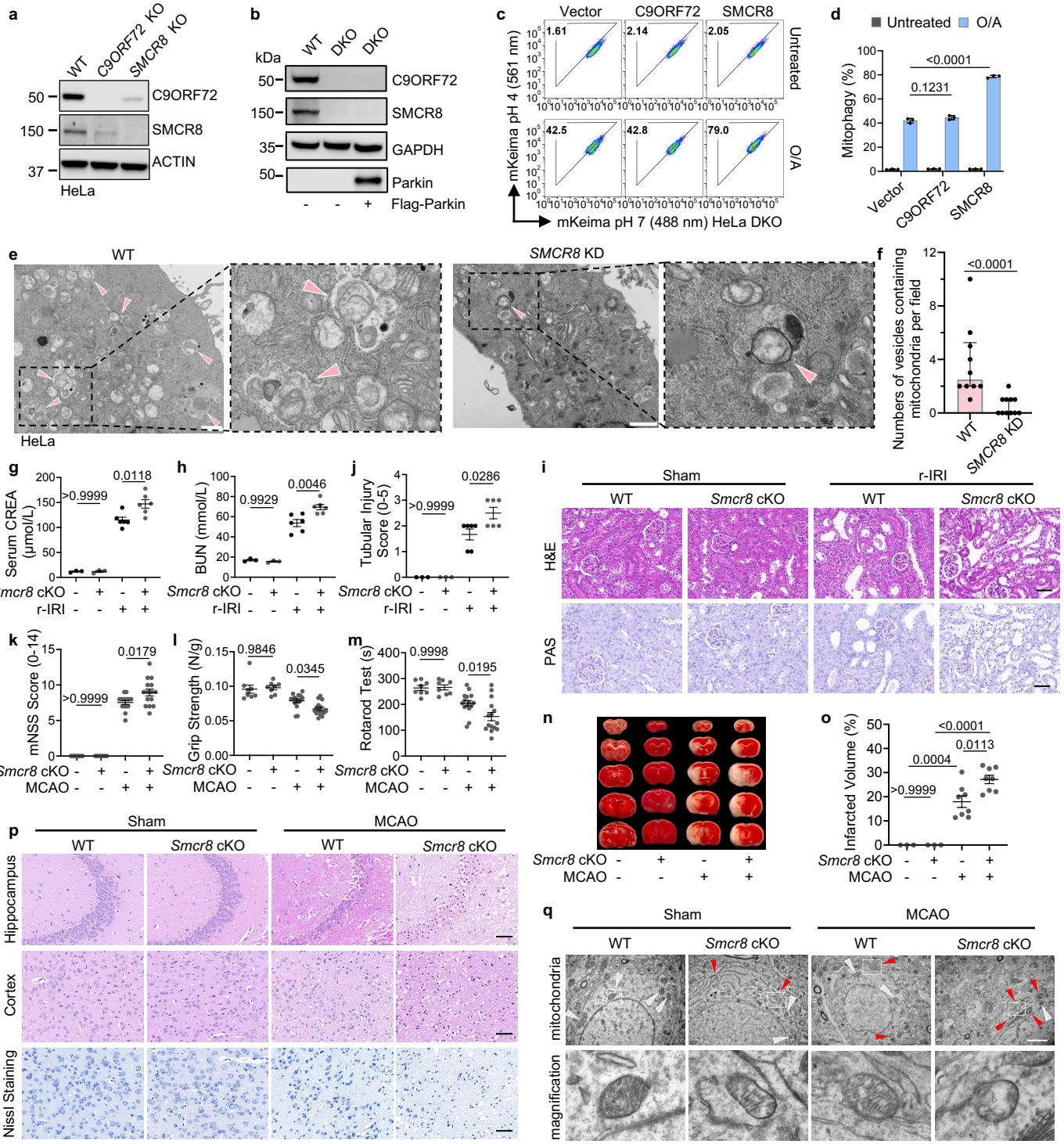
a
WT
C9ORF72 KO
SMCR8 KO
50
C9ORF72
150
SMCR8
37
ACTIN
HeLa
b
kDa
WT
DKO
DKO
50
C9ORF72
150
SMCR8
35
GAPDH
50
Parkin
- - +
Flag-Parkin
c
Vector
C9ORF72
SMCR8
1.61
2.14
2.05
Untreated
42.5
42.8
79.0
O/A
mKeima pH 4 (561 nm)
mKeima pH 7 (488 nm) HeLa DKO
d
Untreated
O/A
Mitophagy (%)
<0.0001
0.1231
Vector
C9ORF72
SMCR8
e
WT
SMCR8 KD
HeLa
f
Numbers of vesicles containing mitochondria per field
<0.0001
WT
SMCR8 KD
g
Serum CREA (μmol/L)
>0.9999
0.0118
Smcr8 cKO
r-IRI
h
BUN (mmol/L)
0.9929
0.0046
j
Tubular Injury Score (0-5)
>0.9999
0.0286
i
Sham
r-IRI
WT
Smcr8 cKO
H&E
PAS
k
mNSS Score (0-14)
>0.9999
0.0179
MCAO
l
Grip Strength (N/g)
0.9846
0.0345
m
Rotarod Test (s)
0.9998
0.0195
n
o
Infarcted Volume (%)
<0.0001
0.0113
0.0004
>0.9999
p
Sham
MCAO
WT
Smcr8 cKO
Hippocampus
Cortex
Nissl Staining
q
Sham
MCAO
WT
Smcr8 cKO
mitochondria
magnification

Figure 2

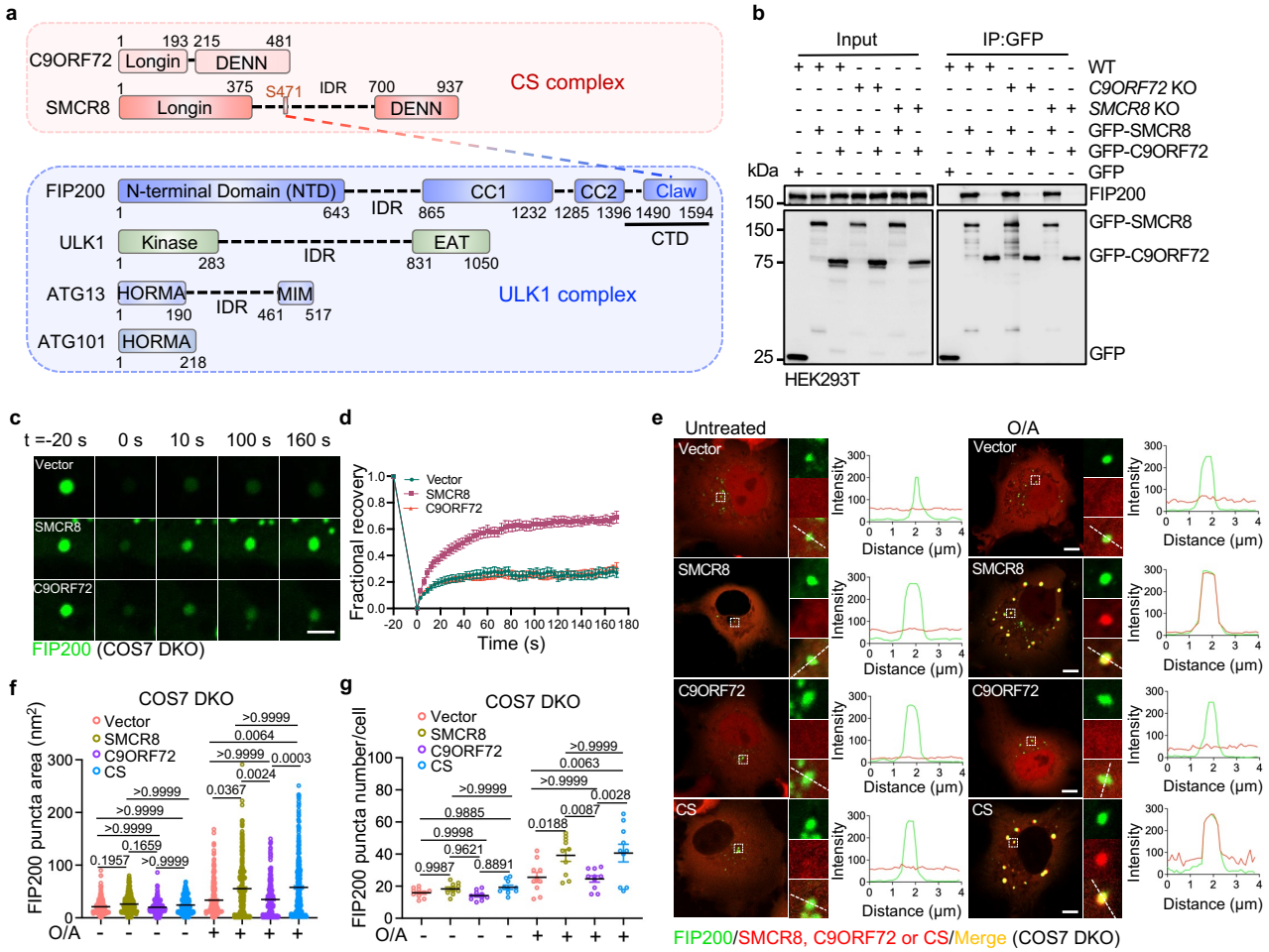
a
C9ORF72
Longin
DENN
SMCR8
S471
IDR
CS complex
FIP200
N-terminal Domain (NTD)
CC1
CC2
Claw
CTD
ULK1
Kinase
EAT
ATG13
HORMA
MIM
ATG101
ULK1 complex
b
Input
IP:GFP
WT
C9ORF72 KO
SMCR8 KO
GFP-SMCR8
GFP-C9ORF72
GFP
kDa
FIP200
HEK293T
c
t =-20 s
0 s
10 s
100 s
160 s
Vector
SMCR8
C9ORF72
FIP200 (COS7 DKO)
d
Fractional recovery
Time (s)
e
Untreated
O/A
Intensity
Distance (μm)
FIP200/SMCR8, C9ORF72 or CS/Merge (COS7 DKO)
f
COS7 DKO
FIP200 puncta area (nm²)
g
FIP200 puncta number/cell

Figure 3

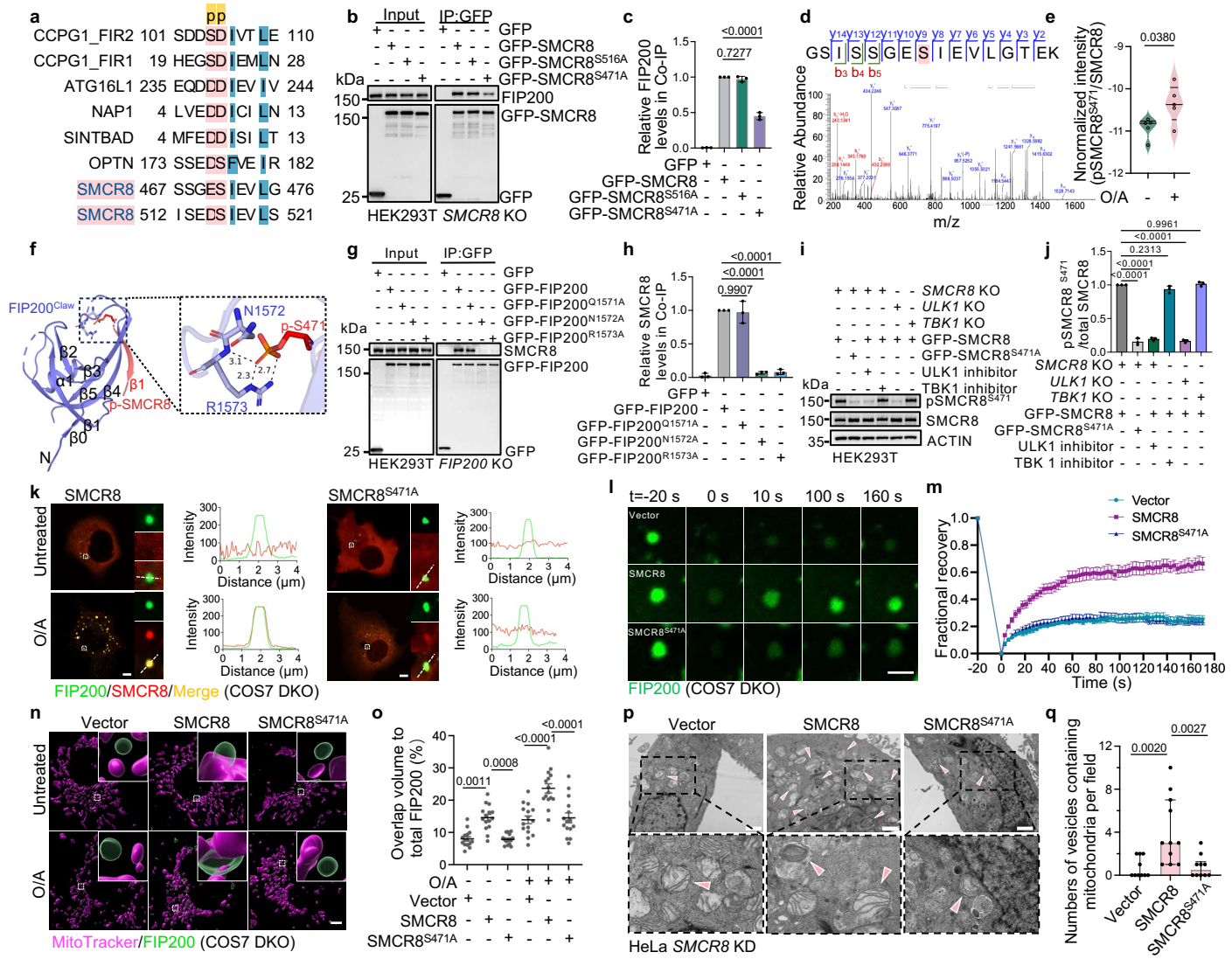
a
pp
CCPG1_FIR2 101 SDDSD IVT LE 110
CCPG1_FIR1 19 HEGSD IEML N 28
ATG16L1 235 EQDDD IEV IV 244
NAP1 4 LVEDD ICI LN 13
SINTBAD 4 MFEDD ISI LT 13
OPTN 173 SSEDS FVE IR 182
SMCR8 467 SSGES IEV LG 476
SMCR8 512 ISEDS IEV LS 521
b
Input
IP:GFP
GFP
GFP-SMCR8
GFP-SMCR8S516A
GFP-SMCR8S471A
kDa
150
150
25
FIP200
GFP-SMCR8
GFP
HEK293T SMCR8 KO
c
<0.0001
0.7277
Relative FIP200 levels in Co-IP
GFP
GFP-SMCR8
GFP-SMCR8S516A
GFP-SMCR8S471A
d
GSISSGESIEVLGTEK
b3 b4 b5
Relative Abundance
m/z
e
0.0380
Nnormalized intensity (pSMCR8S471/SMCR8)
O/A
f
FIP200Claw
N1572
p-S471
3.1
2.3
2.7
β2
α1
β3
β5
β4
β1
p-SMCR8
R1573
β1
β0
N
g
Input
IP:GFP
GFP
GFP-FIP200
GFP-FIP200Q1571A
GFP-FIP200N1572A
GFP-FIP200R1573A
kDa
150
150
25
SMCR8
GFP-FIP200
GFP
HEK293T FIP200 KO
h
<0.0001
<0.0001
0.9907
Relative SMCR8 levels in Co-IP
GFP
GFP-FIP200
GFP-FIP200Q1571A
GFP-FIP200N1572A
GFP-FIP200R1573A
i
SMCR8 KO
ULK1 KO
TBK1 KO
GFP-SMCR8
GFP-SMCR8S471A
ULK1 inhibitor
TBK1 inhibitor
kDa
150
150
35
pSMCR8S471
SMCR8
ACTIN
HEK293T
j
0.9961
<0.0001
0.2313
<0.0001
<0.0001
pSMCR8 S471 /total SMCR8
SMCR8 KO
ULK1 KO
TBK1 KO
GFP-SMCR8
GFP-SMCR8S471A
ULK1 inhibitor
TBK 1 inhibitor
k
SMCR8
SMCR8S471A
Untreated
O/A
Intensity
Distance (μm)
FIP200/SMCR8/Merge (COS7 DKO)
l
t=-20 s
0 s
10 s
100 s
160 s
Vector
SMCR8
SMCR8S471A
FIP200 (COS7 DKO)
m
Vector
SMCR8
SMCR8S471A
Fractional recovery
Time (s)
n
Vector
SMCR8
SMCR8S471A
Untreated
O/A
MitoTracker/FIP200 (COS7 DKO)
o
<0.0001
<0.0001
0.0008
0.0011
Overlap volume to total FIP200 (%)
O/A
Vector
SMCR8
SMCR8S471A
p
Vector
SMCR8
SMCR8S471A
HeLa SMCR8 KD
q
0.0027
0.0020
Numbers of vesicles containing mitochondria per field
Vector
SMCR8
SMCR8S471A

Figure 4

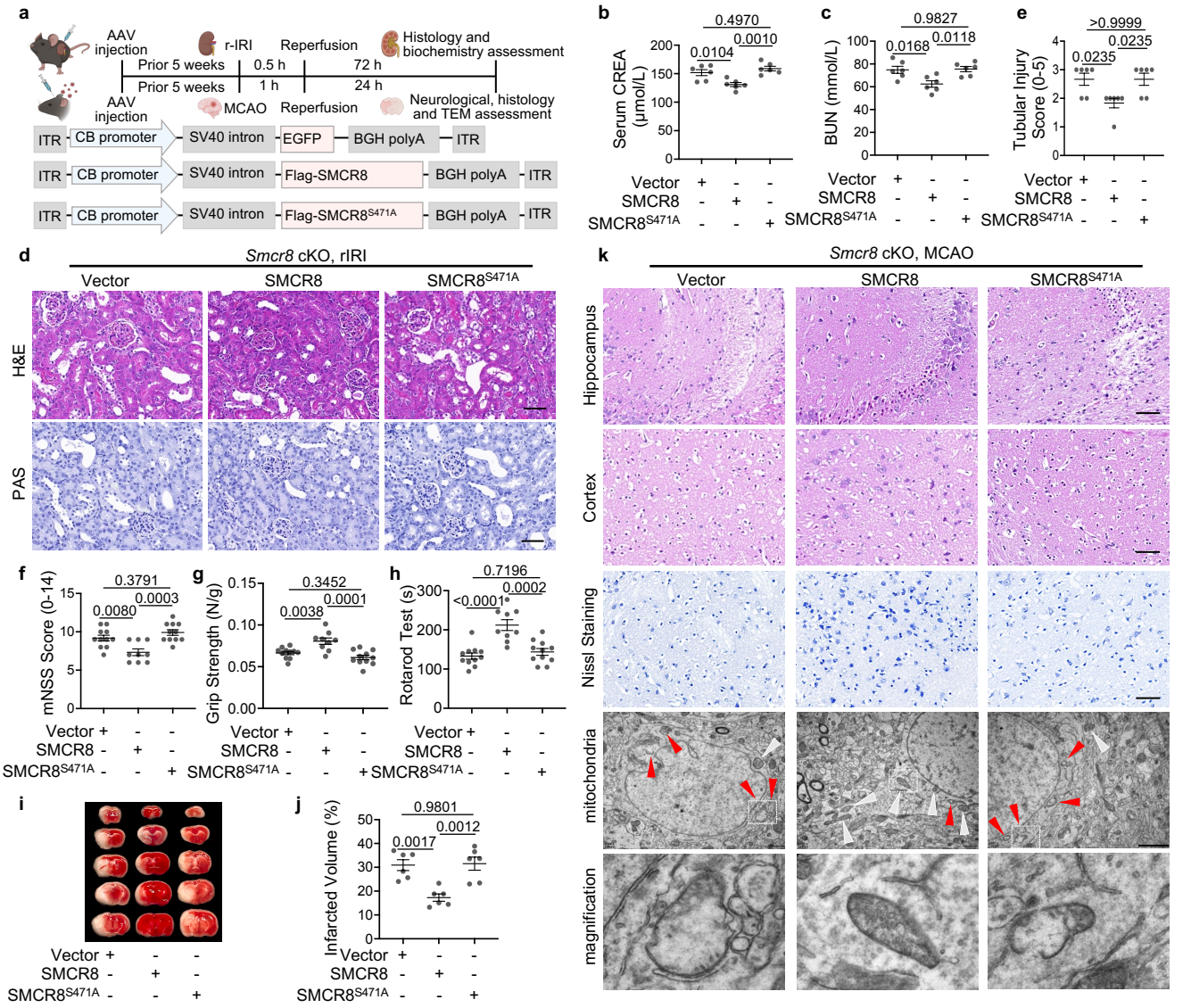
a
AAV injection
r-IRI
Reperfusion
Histology and biochemistry assessment
Prior 5 weeks
0.5 h
72 h
Prior 5 weeks
1 h
24 h
AAV injection
MCAO
Reperfusion
Neurological, histology and TEM assessment
ITR
CB promoter
SV40 intron
EGFP
BGH polyA
ITR
ITR
CB promoter
SV40 intron
Flag-SMCR8
BGH polyA
ITR
ITR
CB promoter
SV40 intron
Flag-SMCR8S471A
BGH polyA
ITR
b
Serum CREA (μmol/L)
0.4970
0.0104
0.0010
c
BUN (mmol/L)
0.9827
0.0168
0.0118
e
Tubular Injury Score (0-5)
>0.9999
0.0235
0.0235
Vector
SMCR8
SMCR8S471A
d
Smcr8 cKO, rIRI
Vector
SMCR8
SMCR8S471A
H&E
PAS
k
Smcr8 cKO, MCAO
Vector
SMCR8
SMCR8S471A
Hippocampus
Cortex
Nissl Staining
mitochondria
magnification
f
mNSS Score (0-14)
0.3791
0.0080
0.0003
g
Grip Strength (N/g)
0.3452
0.0038
0.0001
h
Rotarod Test (s)
0.7196
<0.0001
0.0002
i
j
Infarcted Volume (%)
0.9801
0.0017
0.0012

Figure 5

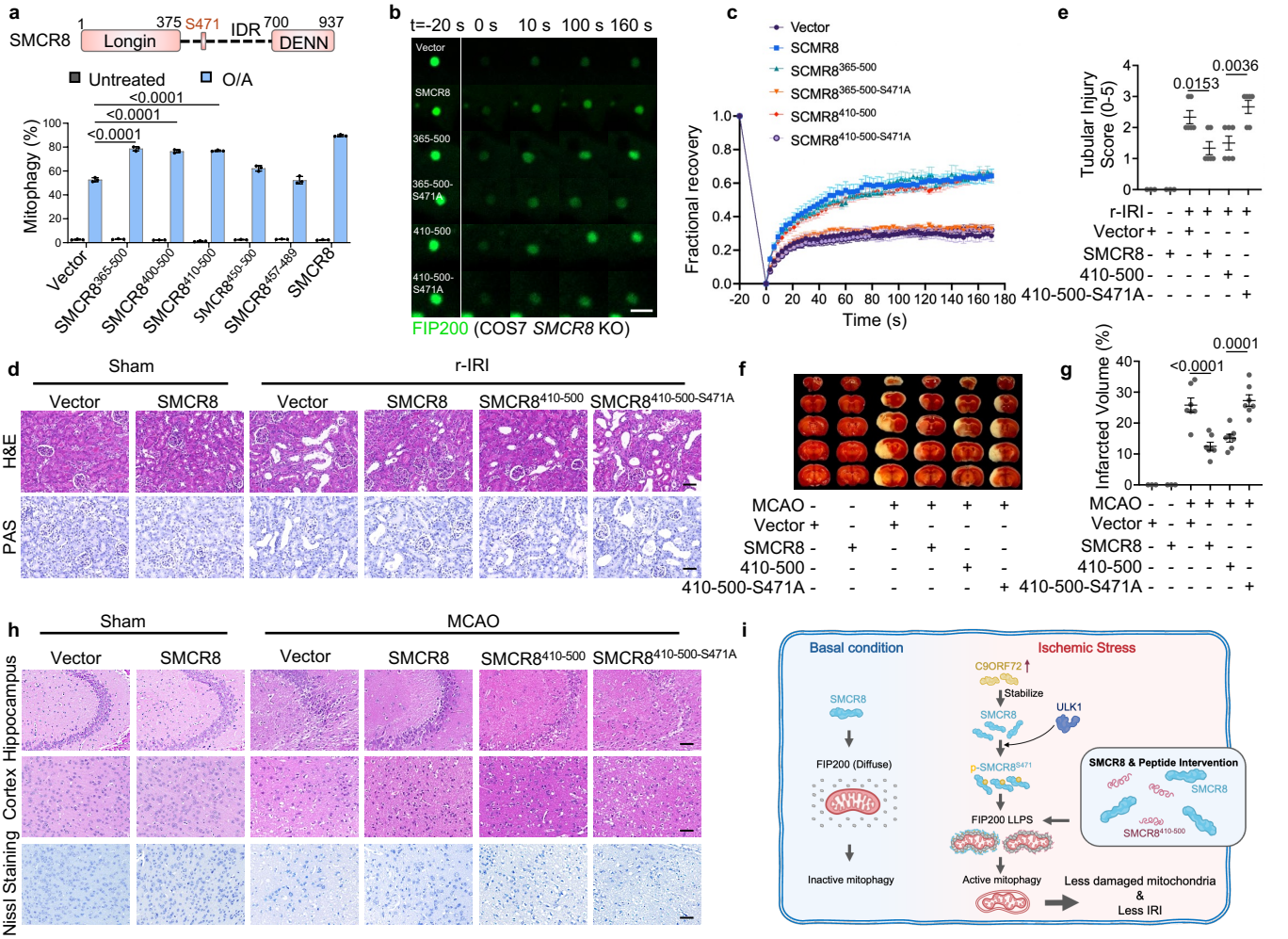
a
SMCR8
Longin
S471
IDR
DENN
Untreated
O/A
Mitophagy (%)
b
t=-20 s 0 s 10 s 100 s 160 s
FIP200 (COS7 SMCR8 KO)
c
Fractional recovery
Time (s)
e
Tubular Injury Score (0-5)
r-IRI
Vector
SMCR8
410-500
410-500-S471A
d
Sham
r-IRI
H&E
PAS
f
MCAO
g
Infarcted Volume (%)
h
Sham
MCAO
Hippocampus
Cortex
Nissl Staining
i
Basal condition
Ischemic Stress
C9ORF72
Stabilize
ULK1
FIP200 (Diffuse)
FIP200 LLPS
Inactive mitophagy
Active mitophagy
SMCR8 & Peptide Intervention
Less damaged mitochondria & Less IRI

Figure 6

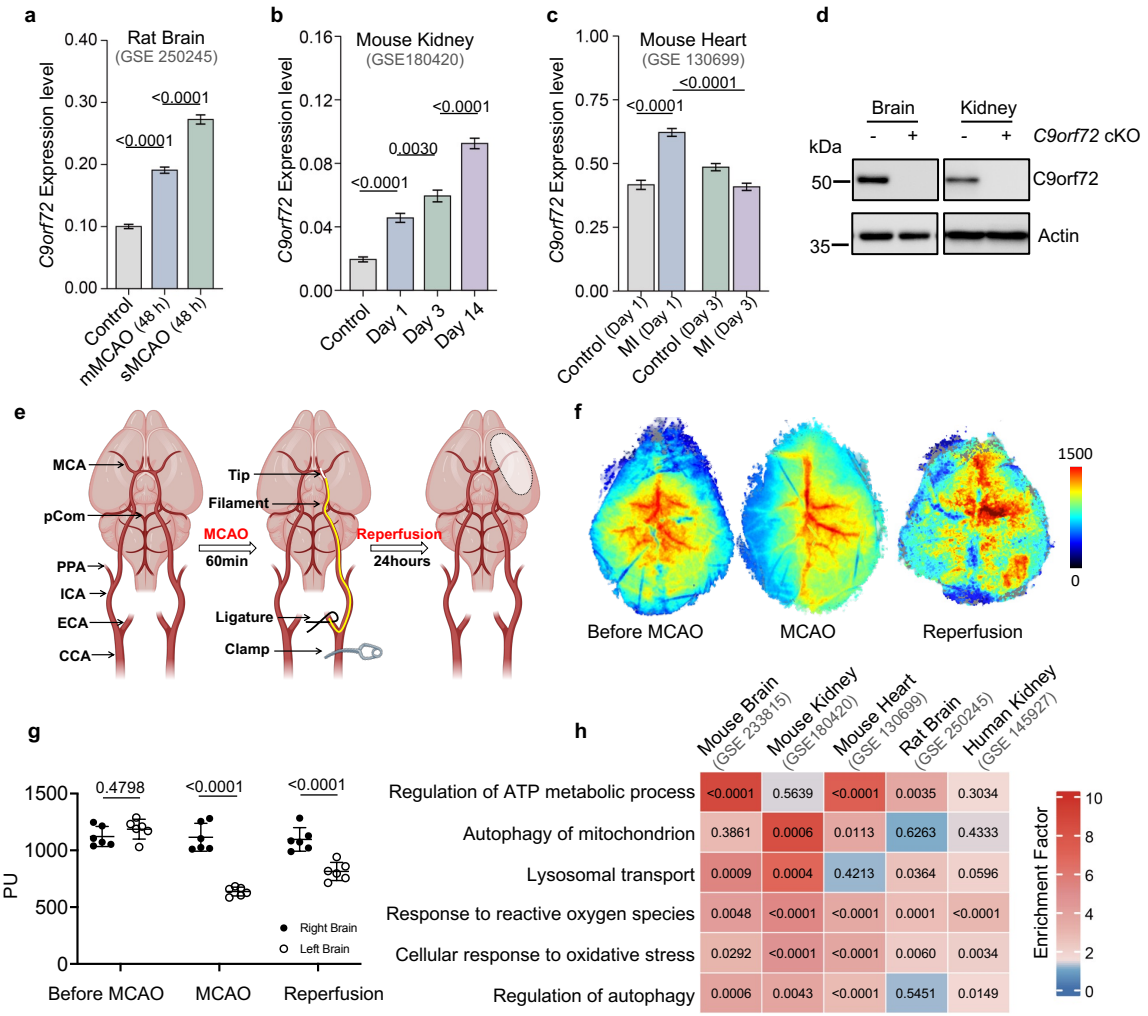
a
Rat Brain
(GSE 250245)
C9orf72 Expression level
<0.0001
<0.0001
Control
mMCAO (48 h)
sMCAO (48 h)
b
Mouse Kidney
(GSE180420)
C9orf72 Expression level
<0.0001
0.0030
<0.0001
Control
Day 1
Day 3
Day 14
c
Mouse Heart
(GSE 130699)
C9orf72 Expression level
<0.0001
<0.0001
Control (Day 1)
MI (Day 1)
Control (Day 3)
MI (Day 3)
d
Brain
Kidney
C9orf72 cKO
kDa
50
35
C9orf72
Actin
e
MCA
pCom
PPA
ICA
ECA
CCA
Tip
Filament
MCAO
60min
Ligature
Clamp
Reperfusion
24hours
f
1500
0
Before MCAO
MCAO
Reperfusion
g
PU
0.4798
<0.0001
<0.0001
Right Brain
Left Brain
Before MCAO
MCAO
Reperfusion
h
Mouse Brain (GSE 233815)
Mouse Kidney (GSE180420)
Mouse Heart (GSE 130699)
Rat Brain (GSE 250245)
Human Kidney (GSE 145927)
Regulation of ATP metabolic process
Autophagy of mitochondrion
Lysosomal transport
Response to reactive oxygen species
Cellular response to oxidative stress
Regulation of autophagy
<0.0001 0.5639 <0.0001 0.0035 0.3034
0.3861 0.0006 0.0113 0.6263 0.4333
0.0009 0.0004 0.4213 0.0364 0.0596
0.0048 <0.0001 <0.0001 0.0001 <0.0001
0.0292 <0.0001 <0.0001 0.0060 0.0034
0.0006 0.0043 <0.0001 0.5451 0.0149
Enrichment Factor
10
8
6
4
2
0

Figure S1

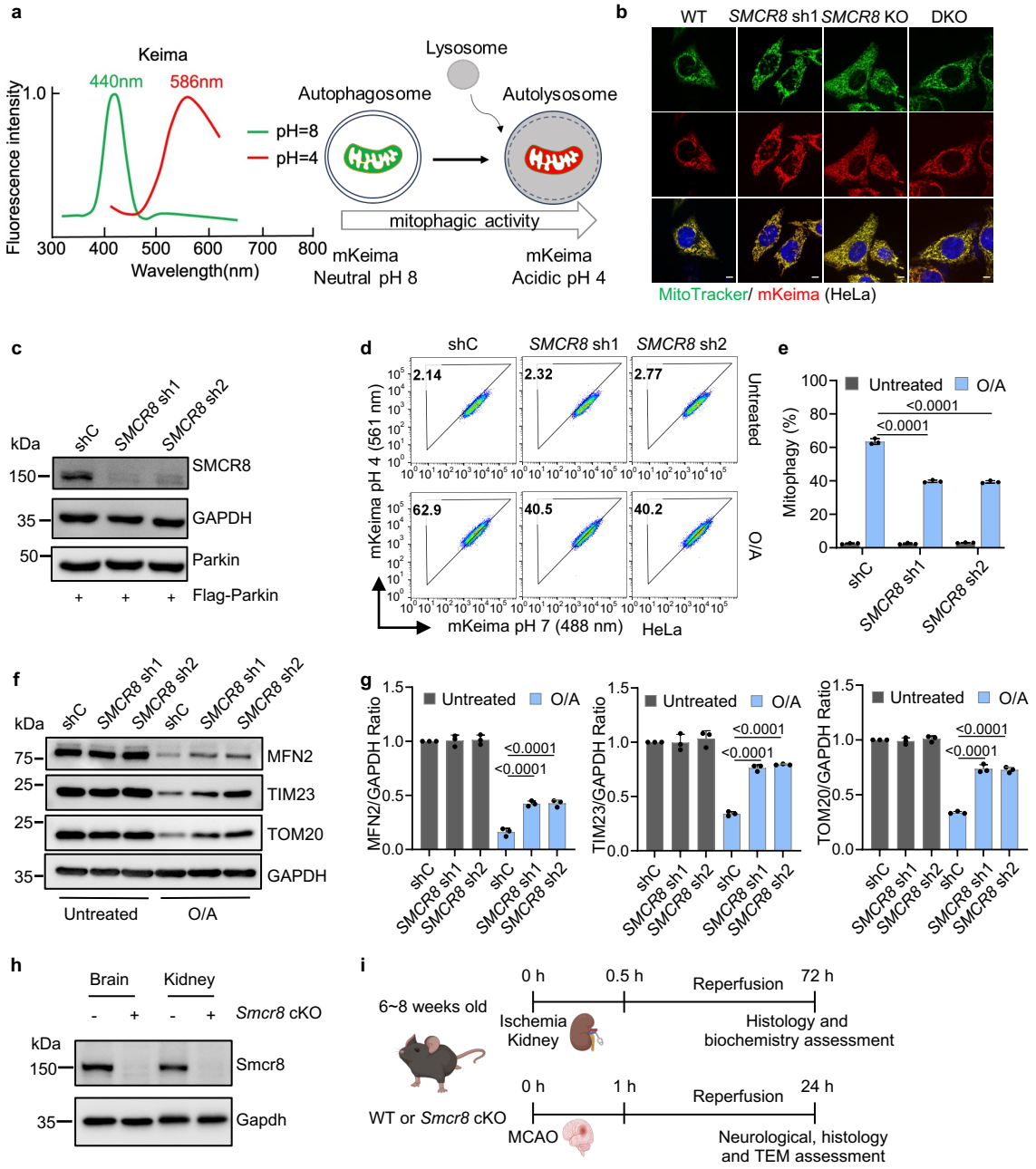
a
Keima
440nm
586nm
1.0
Fluorescence intensity
300 400 500 600 700 800
Wavelength(nm)
pH=8
pH=4
Lysosome
Autophagosome
Autolysosome
mitophagic activity
mKeima
Neutral pH 8
mKeima
Acidic pH 4
b
WT
SMCR8 sh1
SMCR8 KO
DKO
MitoTracker/ mKeima (HeLa)
c
kDa
shC
SMCR8 sh1
SMCR8 sh2
150
SMCR8
35
GAPDH
50
Parkin
+ + +
Flag-Parkin
d
shC
SMCR8 sh1
SMCR8 sh2
2.14
2.32
2.77
62.9
40.5
40.2
Untreated
O/A
mKeima pH 4 (561 nm)
mKeima pH 7 (488 nm)
HeLa
e
Untreated
O/A
Mitophagy (%)
<0.0001
<0.0001
shC
SMCR8 sh1
SMCR8 sh2
f
kDa
shC
SMCR8 sh1
SMCR8 sh2
shC
SMCR8 sh1
SMCR8 sh2
75
MFN2
25
TIM23
25
TOM20
35
GAPDH
Untreated
O/A
g
Untreated
O/A
MFN2/GAPDH Ratio
TIM23/GAPDH Ratio
TOM20/GAPDH Ratio
<0.0001
<0.0001
shC
SMCR8 sh1
SMCR8 sh2
h
Brain
Kidney
Smcr8 cKO
- + - +
kDa
150
Smcr8
35
Gapdh
i
6~8 weeks old
0 h
0.5 h
Reperfusion
72 h
Ischemia
Kidney
Histology and
biochemistry assessment
WT or Smcr8 cKO
0 h
1 h
Reperfusion
24 h
MCAO
Neurological, histology
and TEM assessment

Figure S2

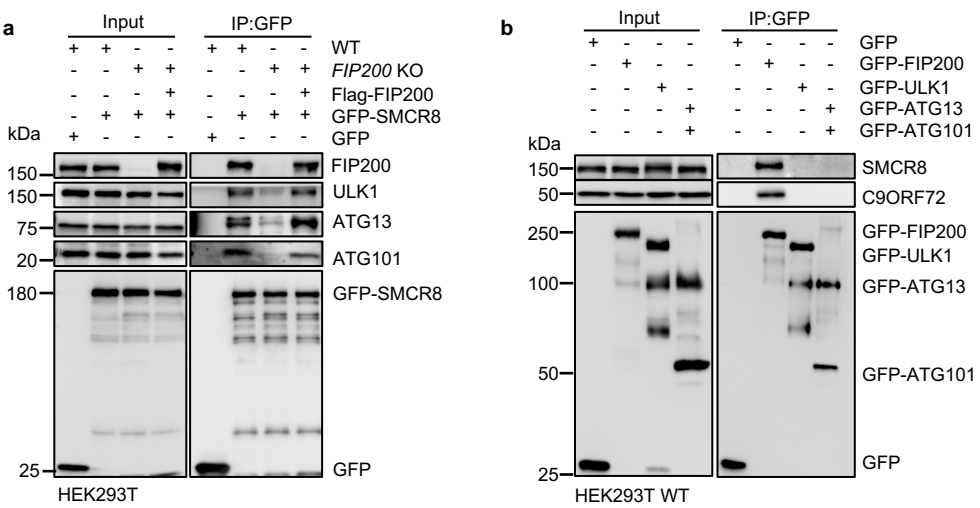
a
Input
IP:GFP
WT
FIP200 KO
Flag-FIP200
GFP-SMCR8
GFP
kDa
150
150
75
20
180
25
FIP200
ULK1
ATG13
ATG101
GFP-SMCR8
GFP
HEK293T
b
Input
IP:GFP
GFP
GFP-FIP200
GFP-ULK1
GFP-ATG13
GFP-ATG101
kDa
150
50
250
100
50
25
SMCR8
C9ORF72
GFP-FIP200
GFP-ULK1
GFP-ATG13
GFP-ATG101
GFP
HEK293T WT

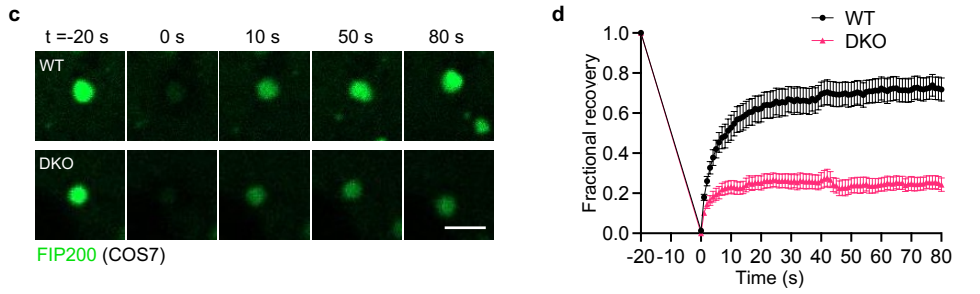
c
t =-20 s
0 s
10 s
50 s
80 s
WT
DKO
FIP200 (COS7)
d
WT
DKO
Fractional recovery
1.0
0.8
0.6
0.4
0.2
0.0
-20 -10 0 10 20 30 40 50 60 70 80
Time (s)

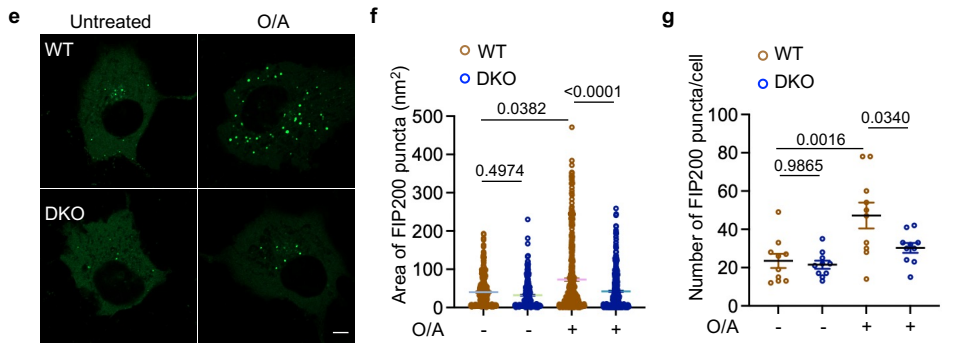
e
Untreated
O/A
WT
DKO
f
WT
DKO
Area of FIP200 puncta (nm2)
0.0382
<0.0001
0.4974
500
400
300
200
100
0
O/A
- - + +
g
WT
DKO
Number of FIP200 puncta/cell
0.0016
0.0340
0.9865
100
80
60
40
20
0
O/A
- - + +

Figure S3

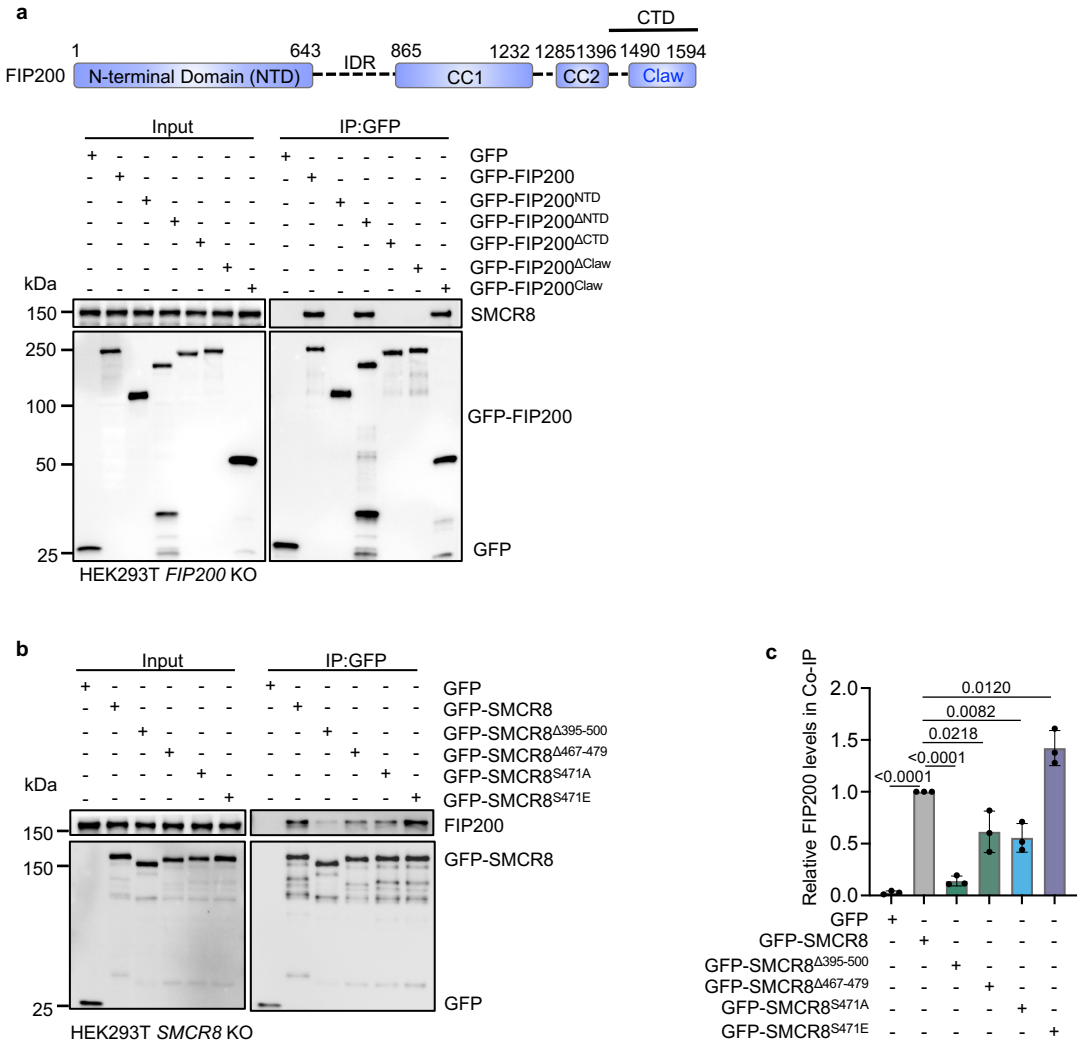
a
CTD
1
643
IDR
865
1232 1285 1396 1490 1594
FIP200
N-terminal Domain (NTD)
CC1
CC2
Claw
Input
IP:GFP
GFP
GFP-FIP200
GFP-FIP200NTD
GFP-FIP200ΔNTD
GFP-FIP200ΔCTD
GFP-FIP200ΔClaw
GFP-FIP200Claw
kDa
150
250
100
50
25
SMCR8
GFP-FIP200
GFP
HEK293T FIP200 KO
b
Input
IP:GFP
GFP
GFP-SMCR8
GFP-SMCR8Δ395-500
GFP-SMCR8Δ467-479
GFP-SMCR8S471A
GFP-SMCR8S471E
kDa
150
150
25
FIP200
GFP-SMCR8
GFP
HEK293T SMCR8 KO
c
Relative FIP200 levels in Co-IP
2.0
1.5
1.0
0.5
0.0
0.0120
0.0082
0.0218
<0.0001
<0.0001
GFP
GFP-SMCR8
GFP-SMCR8Δ395-500
GFP-SMCR8Δ467-479
GFP-SMCR8S471A
GFP-SMCR8S471E

Figure S4

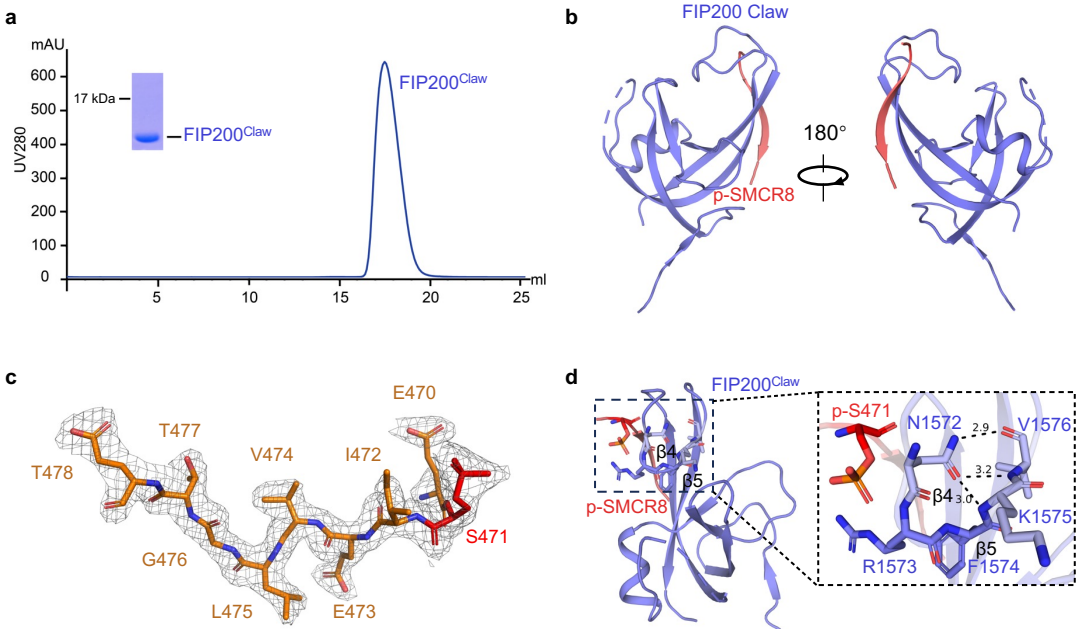
a
mAU
600
500
400
300
200
100
0
UV280
17 kDa
FIP200Claw
FIP200Claw
5
10
15
20
25
ml
b
FIP200 Claw
180°
p-SMCR8
c
E470
T477
T478
V474
I472
S471
G476
L475
E473
d
FIP200Claw
p-S471
N1572
2.9
V1576
β4
β5
3.2
3.0
β4
K1575
β5
p-SMCR8
R1573
F1574

Figure S5

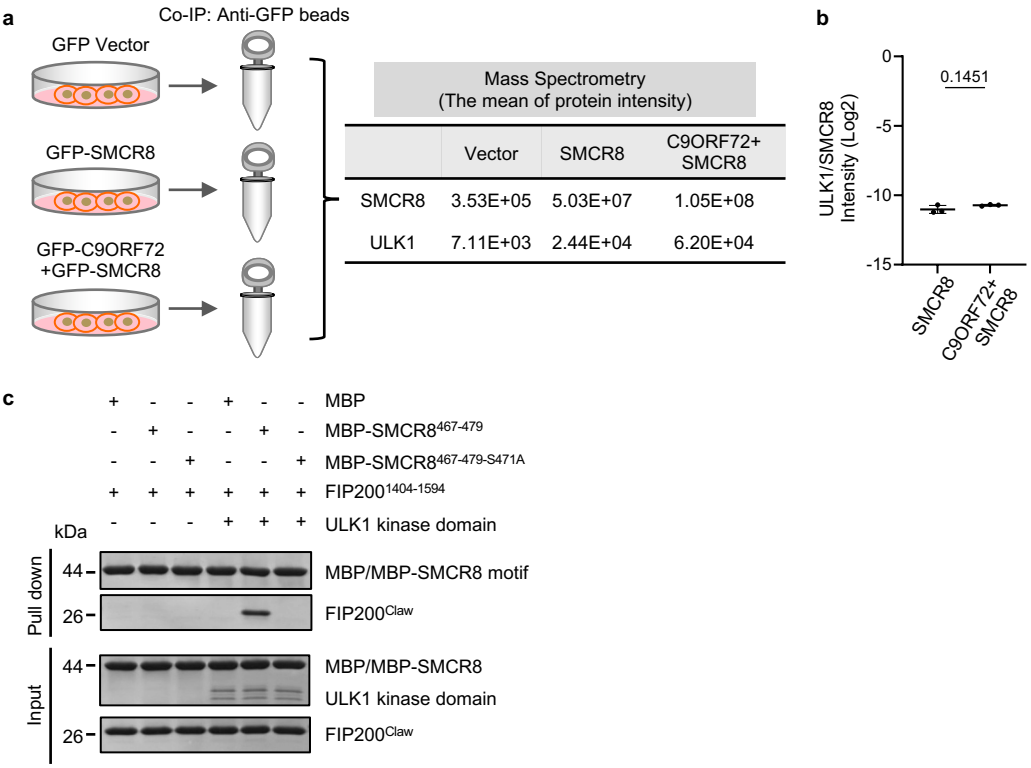
a
Co-IP: Anti-GFP beads
GFP Vector
GFP-SMCR8
GFP-C9ORF72
+GFP-SMCR8
Mass Spectrometry
(The mean of protein intensity)
Vector
SMCR8
C9ORF72+
SMCR8
SMCR8 3.53E+05 5.03E+07 1.05E+08
ULK1 7.11E+03 2.44E+04 6.20E+04
b
ULK1/SMCR8
Intensity (Log2)
0
-5
-10
-15
0.1451
SMCR8
C9ORF72+
SMCR8
c
MBP
MBP-SMCR8467-479
MBP-SMCR8467-479-S471A
FIP2001404-1594
ULK1 kinase domain
kDa
Pull down
44
26
MBP/MBP-SMCR8 motif
FIP200Claw
Input
44
MBP/MBP-SMCR8
ULK1 kinase domain
26
FIP200Claw

Figure S6

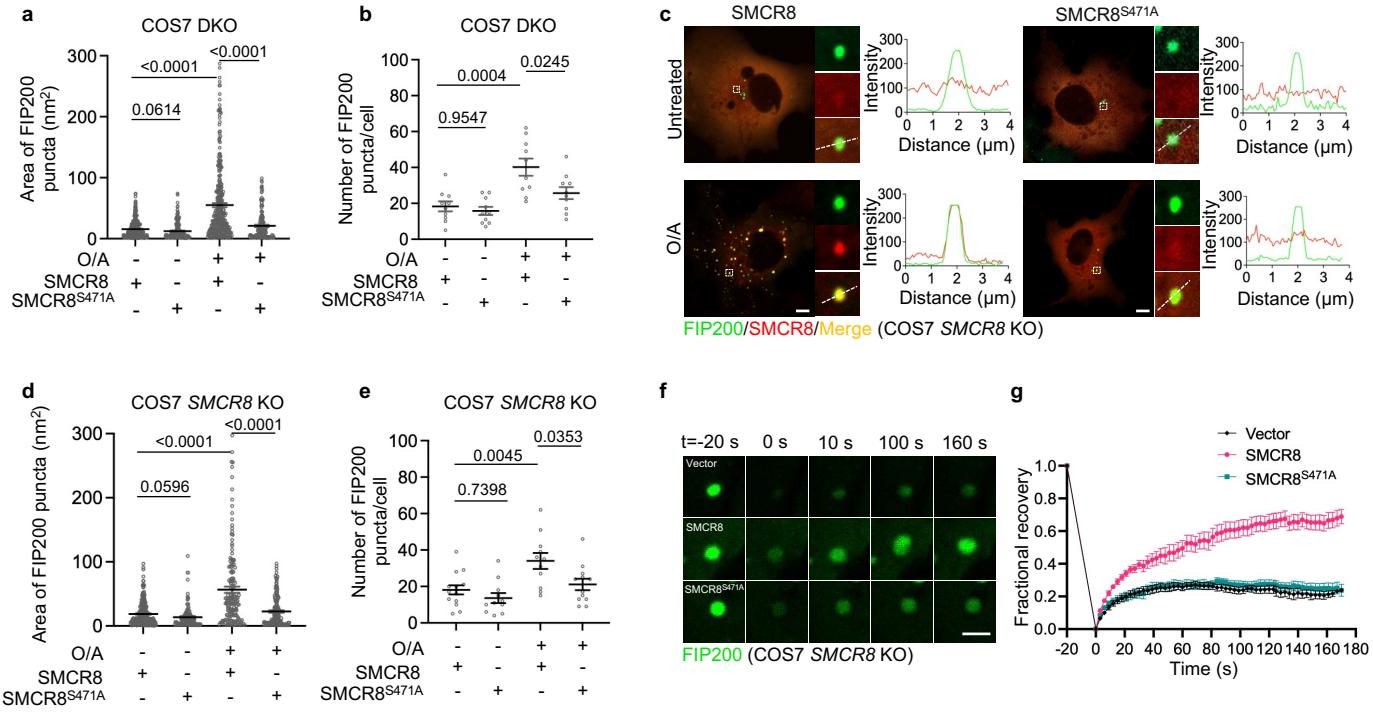
a
COS7 DKO
Area of FIP200 puncta (nm²)
<0.0001
<0.0001
0.0614
O/A
SMCR8
SMCR8S471A
b
COS7 DKO
Number of FIP200 puncta/cell
0.0004
0.0245
0.9547
c
SMCR8
SMCR8S471A
Untreated
O/A
Intensity
Distance (μm)
FIP200/SMCR8/Merge (COS7 SMCR8 KO)
d
COS7 SMCR8 KO
Area of FIP200 puncta (nm²)
<0.0001
<0.0001
0.0596
e
COS7 SMCR8 KO
Number of FIP200 puncta/cell
0.0045
0.0353
0.7398
f
t=-20 s
0 s
10 s
100 s
160 s
Vector
SMCR8
SMCR8S471A
FIP200 (COS7 SMCR8 KO)
g
Vector
SMCR8
SMCR8S471A
Fractional recovery
Time (s)

Figure S7

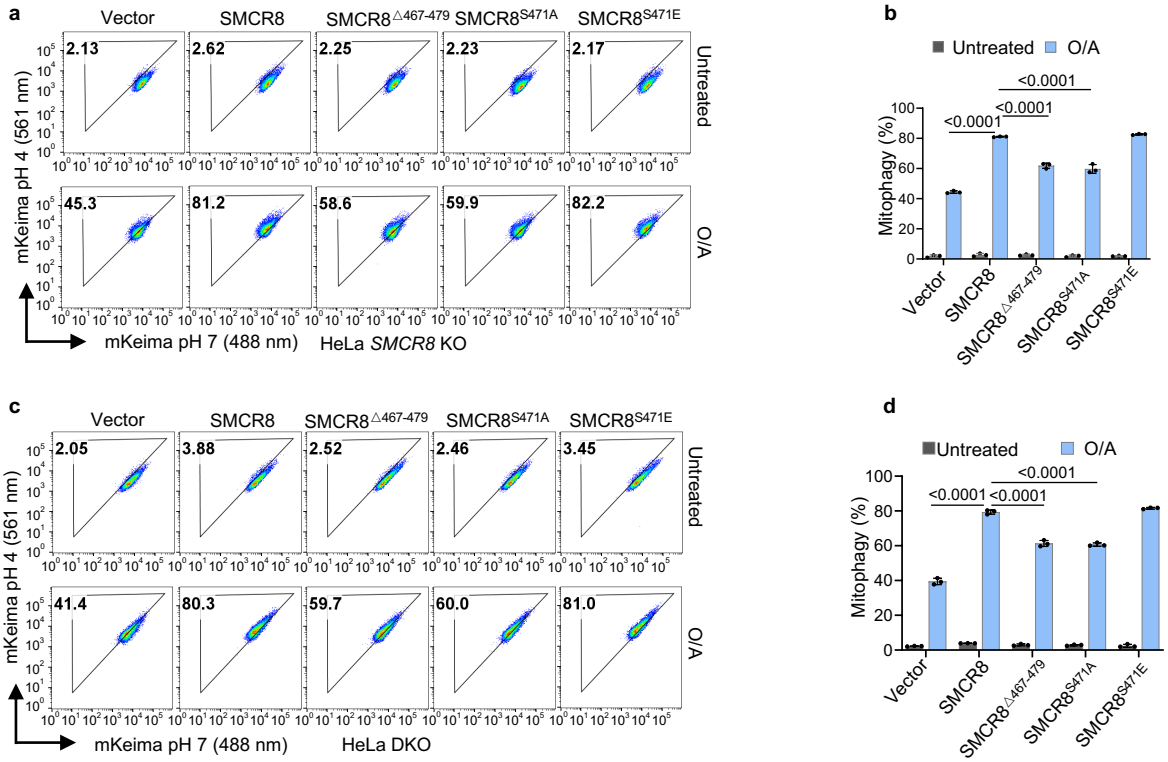
a
Vector
SMCR8
SMCR8△467-479
SMCR8S471A
SMCR8S471E
Untreated
O/A
2.13
2.62
2.25
2.23
2.17
45.3
81.2
58.6
59.9
82.2
mKeima pH 4 (561 nm)
mKeima pH 7 (488 nm)
HeLa SMCR8 KO
b
Untreated
O/A
Mitophagy (%)
<0.0001
<0.0001
<0.0001
Vector
SMCR8
SMCR8△467-479
SMCR8S471A
SMCR8S471E
c
Vector
SMCR8
SMCR8△467-479
SMCR8S471A
SMCR8S471E
Untreated
O/A
2.05
3.88
2.52
2.46
3.45
41.4
80.3
59.7
60.0
81.0
mKeima pH 4 (561 nm)
mKeima pH 7 (488 nm)
HeLa DKO
d
Untreated
O/A
Mitophagy (%)
<0.0001
<0.0001
<0.0001
Vector
SMCR8
SMCR8△467-479
SMCR8S471A
SMCR8S471E

Figure S8

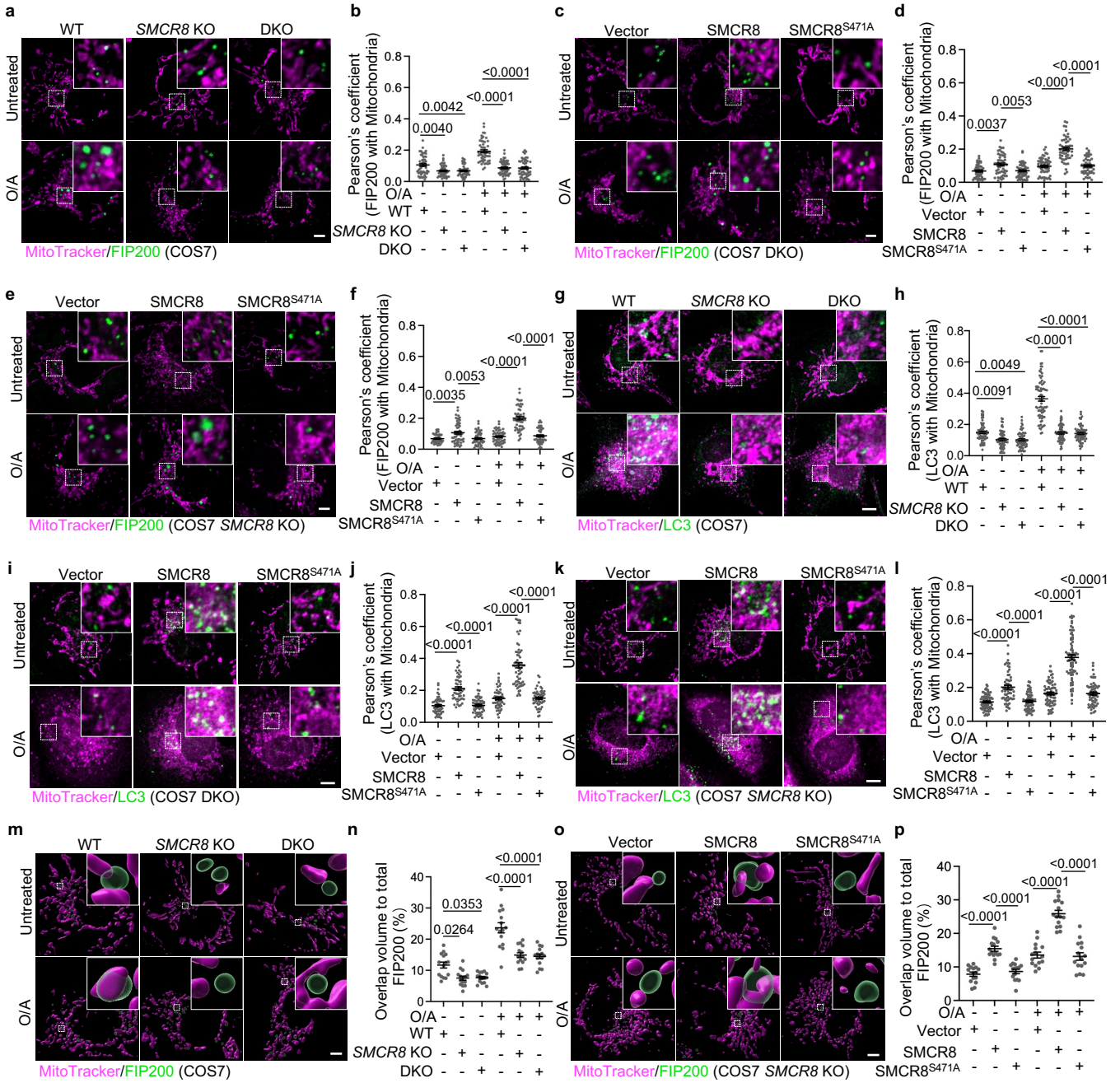
a
WT
SMCR8 KO
DKO
Untreated
O/A
MitoTracker/FIP200 (COS7)
b
Pearson's coefficient (FIP200 with Mitochondria)
0.0040
0.0042
<0.0001
<0.0001
O/A
WT
SMCR8 KO
DKO
c
Vector
SMCR8
SMCR8S471A
MitoTracker/FIP200 (COS7 DKO)
d
0.0037
0.0053
<0.0001
<0.0001
Vector
SMCR8
SMCR8S471A
e
MitoTracker/FIP200 (COS7 SMCR8 KO)
f
0.0035
0.0053
<0.0001
<0.0001
g
MitoTracker/LC3 (COS7)
h
Pearson's coefficient (LC3 with Mitochondria)
0.0091
0.0049
i
MitoTracker/LC3 (COS7 DKO)
j
k
MitoTracker/LC3 (COS7 SMCR8 KO)
l
m
MitoTracker/FIP200 (COS7)
n
Overlap volume to total FIP200 (%)
0.0264
0.0353
o
MitoTracker/FIP200 (COS7 SMCR8 KO)
p

Figure S9

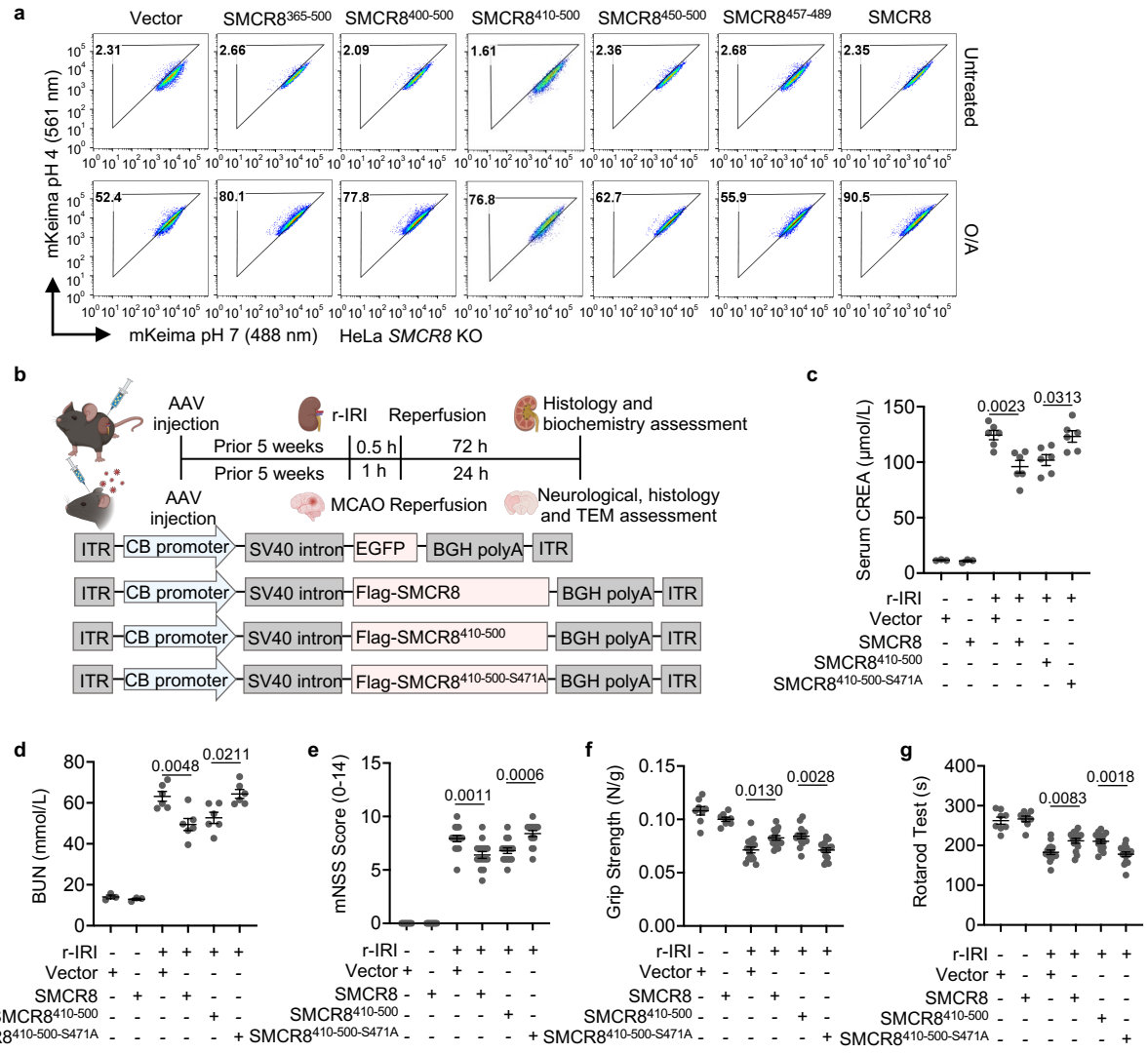
a
Vector
SMCR8365-500
SMCR8400-500
SMCR8410-500
SMCR8450-500
SMCR8457-489
SMCR8
Untreated
O/A
mKeima pH 4 (561 nm)
mKeima pH 7 (488 nm)
HeLa SMCR8 KO
2.31
2.66
2.09
1.61
2.36
2.68
2.35
52.4
80.1
77.8
76.8
62.7
55.9
90.5
b
AAV injection
r-IRI
Reperfusion
Histology and biochemistry assessment
Prior 5 weeks
0.5 h
72 h
Prior 5 weeks
1 h
24 h
AAV injection
MCAO Reperfusion
Neurological, histology and TEM assessment
ITR
CB promoter
SV40 intron
EGFP
BGH polyA
Flag-SMCR8
Flag-SMCR8410-500
Flag-SMCR8410-500-S471A
c
Serum CREA (μmol/L)
0.0023
0.0313
r-IRI
Vector
SMCR8
SMCR8410-500
SMCR8410-500-S471A
d
BUN (mmol/L)
0.0048
0.0211
e
mNSS Score (0-14)
0.0011
0.0006
f
Grip Strength (N/g)
0.0130
0.0028
g
Rotarod Test (s)
0.0083
0.0018

Figure S10